Ring Resonator Photonic Sensing Device

by

Andrew Llewellyn Evans

A thesis
presented to the University of Waterloo
in fulfilment of the
thesis requirement for the degree of
Masters of Science
in
Physics

Waterloo, Ontario, Canada, 2015

This thesis consists of material all of which I authored or co-authored: see Statement of Contributions included in the thesis. This is a true copy of the thesis, including any required final revisions, as accepted by my examiners.

I understand that my thesis may be made electronically available to the public.

Statement of Contributions

The work presented in this thesis was done so under the co-supervision of doctors David Yevick and Paul Jessop. The facilities used to perform the sensor testing was provided by Wilfrid Laurier University.

The sensor chip tested in this thesis was designed by Jason Ackert and provided by Andrew Knights lab at McMaster University. One script used in the data collection was written by Andrew Knights' lab at McMaster University.

Abstract

This thesis studies a micro ring resonator sensor structure built using the silicon-on-insulator (SOI) platform. The sensor detects changes in index of refraction with a sensitivity of 21 nm/RIU (RIU stands for refractive index unit), in close agreement to the predicted sensitivity, from computer simulations, of 24.4 nm/RIU. A study of thermal effects and residue layers was performed and a future sensor design capable of measuring layer thickness during evaporation is proposed.

Background material relevant to the modelling of passive optical devices and a general overview of sensor design is presented. The sensitivity of various waveguide structures to changes in cover index of refraction are studied using computer simulations. The change in free spectral range (FSR) of the resonator sensor was characterized and was used to extend the active range of the device.

Acknowledgements

I would like to thank my supervisors David Yevick and Paul Jessop. You gave me motivation and direction whenever I was tired and lost. Your pragmatism and wealth of experience helped me navigate the nebulous path toward the completion of this thesis.

Rajit Day, I learned all that I know of lab work in the field of photonics from you. Your stories of endless frustration from dealing with light couplers put my own problems in perspective.

Thank You Jason Ackert for designing the SOI chip used as the sensor in this thesis and to Andrew Knights for allowing me to use it.

George Soliman, you made being in the lab fun. The welcome distractions we provided each other with kept me sane.

Eric Campbell, thank you for proofreading the body of this thesis. Your keen linguistic insight supplemented my lack gooder grammar.

Lastly, Judy McDonnell, thank you for putting up with my hatred of paperwork.

Dedicated to my late pets; Templeton and Greer

Contents

List of Figures

List of Abbreviations

SOI:	Silicon on Insulator
EM:	Electro Magnetic
DE:	Differential Equation
PDE:	Partial Differential Equation
TE:	Transverse Electric
TM:	Transverse Magnetic
RIU:	Refractive Index Unit
FDTD:	Finite Difference Time Domain
BEAMPROP:	Beam Propagation
FSR:	Free Spectral Range

1 Introduction

1.1 Silicon on Insulator (SOI) Chips

Semiconductor design and manufacture has been one of the most researched areas of the last 50 years and is pervasive in all modern technology. Semiconductor manufacturing processes are also employed to produce chips that transmit optical, instead of electrical, power. Highly developed manufacturing techniques enable operation at performance limits while minimizing form factor and device feature size.

The fabrication of SOI devices starts with the production of large, high purity, silicon crystals. Cooling a liquid state sample is not practical because thermal stresses cause defects. A more complex method, the Czochralski method, has made the mass production of high quality crystals possible. In the Czochralski method a starter crystal, which is cleaved and carefully oriented along its crystal axis, is dipped in a sample of molten silicon. The starter crystal is slowly pulled upward allowing for the formation of new crystal structure below the cleaved starter due to the surface tension of the liquid surface. The pull rate, rotation rate, and the temperature gradient during cooling are all chosen to maximise the purity of the product.

Once the bulk crystal has been produced it is cut into thin wafers and the oxide layer, which has a lower index of refraction than silicon, is produced. The oxide layer is made after the cleaving process either by bonding an oxidised wafer to an unoxidised one, or using ion implantation and annealing. In either case, the product is a three layer structure composed of Si, SiO_2, and Si, all with precise thicknesses. The fabrication of waveguide structures is done by carefully controlling which regions of the Si crystal are exposed to the effects of various steps in the manufacturing step. A polymer cover is first applied to the whole chip and then areas are selectively exposed to ultraviolet light. The exposed areas are chemically altered when interacting with ultraviolet light. Then, depending on the polymer and the solvent used, either the exposed or unexposed regions of the cover are removed. The remaining polymer components act as a barrier for the effects of the manufacturing step, such as ion implantation, chemical etching, or vapour deposition. The remaining polymer is then removed and the process is repeated until the structure is fully fabricated.

1.2 Sensing Devices

Sensors are a ubiquitous part of modern society. In industrial processes, knowledge of the environment or chemical properties critically impacts production efficiency. There has always been a need for the development of new sensors, with precision, portability, and power consumption being the driving factors. Commonly used structures in the optical communication field can be adapted to become sensors if the response to changes in environment can be characterized. The highly developed manufacturing techniques allow for highly sensitive SOI sensors to be realized with a small physical footprint and low power consumption.

Sensors quantify a particular environmental property value, the measurand, through changes in the transmission spectrum of the sensing device. They can be used to, among other things, track chemical reaction rates, detect viruses, or measure material stress depending on the waveguide structure used as the sensor. Attaining higher accuracy makes the area of sensor design a constantly active area of research. With the SOI platform, various structures can be devised to exploit phenomena creating

unique transmission spectra. Interferometer, resonator, bending loss, and surface plasmon resonance sensors can all be realized using the SOI platform.

1.3 Goal

In this thesis a resonator structure will be employed as a sensor for changes in refractive indices. Changes in the cover index of refraction affect the nature of the bound modes supported by the waveguide structure and therefore the transmission spectrum of the device. This effect is characterized through computer simulations and the predicted sensitivity can be compared to the measured value for the device used in the tests. The effects of temperature change, caused by an evaporating sample, as well as residues deposited by evaporating samples, are studied. Using the conclusions drawn from these studies, a model of a sensor that could measure surface layer thickness of a sample during evaporation is devised.

This thesis is organized as follows. To begin, background information regarding guided waves and passive optical devices is given. Various methods of mode calculation and passive structures, as well as computational tools used to analyse them, will be discussed. Next, the predicted performance of a ring resonator sensor is calculated using computer simulation data. The ring structure is then tested and the sensitivity of the device is determined. Possible future work is presented along with a brief look into current sensor design and sensitivity.

2 Background Theory

2.1 Optical Propagation in Waveguide Structures

Waveguide Structures

The critical concept behind the design of waveguide structures is to have a material with a large index of refraction (relative to the surroundings), shaped in such a way as to allow standing electromagnetic waves to form. When this occurs the frequency of light, waveguide geometry, and values of refractive indices dictate the nature and number of modes a particular structure can support. The analysis of these structures has been examined thoroughly in literature and a brief summery will be presented here. The most commonly used structures that support guided modes are the buried, strip, rib and fibre (shown in Figure 1). These waveguide structures continue to make up the vast majority of waveguides in the field of optical communications.

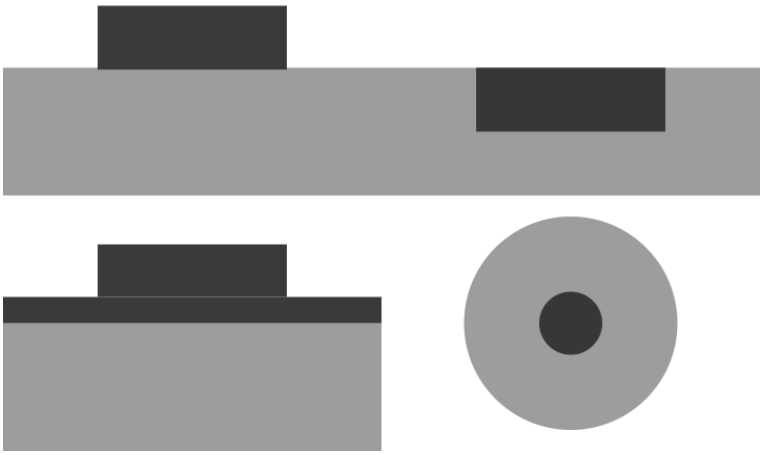

Figure 1: Cross-Section of waveguide structures.
Strip, Buried, Rib and Fibre. High index regions marked in dark areas.

Ray Patterns in Three-Layer Planar Waveguide

The simplest interpretation of guided modes in three slab waveguides is provided by ray tracing and internal reflection. Though a range of angles are subject to internal reflection in a slab waveguide, only the angles that provide paths whose phase difference leads to constructive interference after two reflections form the bound modes. Since total internal reflection is critical to the formation of modes, the index of refraction in region 2 of Figure 2 must be larger than that of its surroundings. The analysis below, described by Figure 2, is two dimensional with the guiding structure being invariant in the x direction. The mode propagates in the z direction and the dielectric is stacked in the y direction.

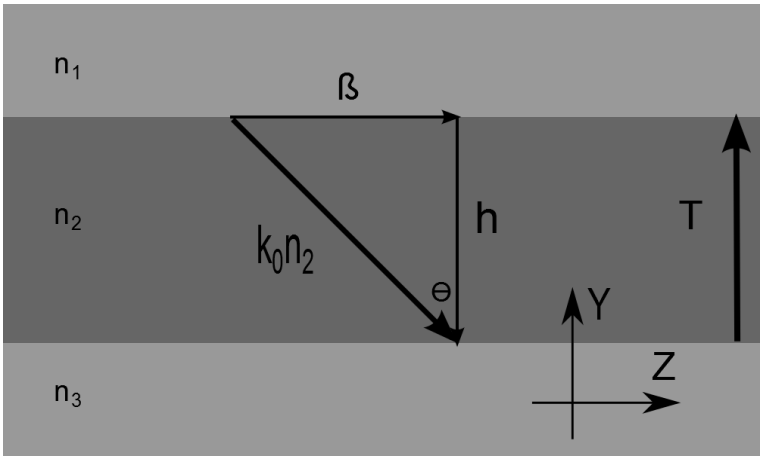

Figure 2: Diagram of three layer slab waveguide.
High index area, n_2, indicated by darker region.

For rays that satisfy the condition for constructive interference, the propagation constant for the mode is related to the free space wavelength by $\beta = n_2 k_0 \sin(\theta)$ where β is the component of the wave vector in the direction of the propagation of the mode. The transverse dependence of the mode is $h = n_2 k_0 \cos(\theta)$ through a similar geometric argument. The dependence of the propagation constant on the free space wavelength is called the dispersion relation.

The polarization of light can be examined at this point. A transverse electric (TE) wave has no electric field component in the direction of the modal field propagation. Likewise, a transverse magnetic (TM) wave has no magnetic field component in the propagation direction. Because of the different interactions of the tangential electric and magnetic fields at the dielectric boundary, these two types of modes behave slightly differently there. A superposition of TE and TM modes can create any EM field distribution.

A plane TE wave bound by the guiding structure in Figure 2, with the assumed electric field component of $E_x(x) = \exp(i(\omega t - \beta z - hx))$, propagating through the waveguide in the z direction would accumulate a total phase of $\omega dt - \beta dz - 2hT + 2\Phi$ over two reflections. The mode travels a distance dz during a time dt over the two reflections, T is the total thickness of the waveguide structure and Φ is the Fresnel phase shift from reflection. Φ depends on the ratio of refractive indices at the boundary and is given by equations (1) and (2) for TM and TE modes respectively. We know that for a mode travelling in the z direction, $wdt - \beta dz = 0$ by the definition of phase velocity. This leads to the relation $2hT + 2\Phi = 2\mathrm{m}\,\pi$ describing constructive interference for modes formed by reflecting rays. Here m is the mode number, n is given by equation (3). From [1].

$$\boldsymbol{\phi_{TM}} = \begin{cases} \boldsymbol{\pi}; & \boldsymbol{\theta < \theta'_P} \\ \boldsymbol{0}; & \boldsymbol{\theta'_p < \theta < \theta_C} \\ \boldsymbol{2\,tan^{-1}\left(\frac{\sqrt{sin^2\,\theta - n^2}}{n^2\,cos\,\theta}\right)}; & \boldsymbol{\theta > \theta_c} \end{cases} \quad (1)$$

$$\boldsymbol{\phi_{TE}} = \begin{cases} \boldsymbol{0}; & \boldsymbol{\theta < \theta_c} \\ \boldsymbol{2\,tan^{-1}\left(\frac{\sqrt{sin^2\,\theta - n^2}}{cos\,\theta}\right)}; & \boldsymbol{\theta > \theta_c} \end{cases} \quad (2)$$

$$\boldsymbol{n = \frac{n_1}{n_2}} \quad (3)$$

The sum $2hT + 2\Phi$ relates the high index material and its thickness to the internal reflection angle, θ, required to generate the mode. Different integers of m (the mode number) produce the bound modes of the structure. Since k_0 depends on the free space wavelength, $\lambda = 2\pi/k_0$, a single waveguide structure will support a spectrum of bound modes, each with their own corresponding free space wavelength and propagation constant.

Maxwell's Equations in Planar Waveguide Structure

Now we seek to analyse bound modes in Figure 2 using Maxwell's equations. In the planar waveguide structure, modes will propagate in the $y - z$ plane and, by symmetry, their propagation properties will be the same for an isotropic medium. The invariant nature of the dielectric in this plane means that any wave propagating in the z direction will have no variation in its EM field components in the y direction - all derivatives with respect to y are zero. The converse is also true for a wave propagating in the y direction. The two curl Maxwell's equations, assuming the electric field behaves as equation (4), produce equations (5) through (10), from [2]:

$$\boldsymbol{E_i(r,t) = E_i(x,y)e^{i(\omega t - \beta z)};\ \ i \in (x,y,z)} \quad (4)$$

$$\boldsymbol{\frac{\partial}{\partial y}E_z + i\beta E_y = -i\omega\mu_0 H_x} \quad (5)$$

$$\boldsymbol{-i\beta E_x - \frac{\partial}{\partial x}E_z = -i\omega\mu_0 H_y} \quad (6)$$

$$\boldsymbol{\frac{\partial}{\partial x}E_y - \frac{\partial}{\partial y}E_x = -i\omega\mu_0 H_z} \quad (7)$$

$$\boldsymbol{\frac{\partial}{\partial y}H_z + i\beta H_y = i\omega\varepsilon_0\varepsilon_r E_x} \quad (8)$$

$$\boldsymbol{-i\beta H_x - \frac{\partial}{\partial x}H_z = i\omega\varepsilon_0\varepsilon_r E_y} \quad (9)$$

$$\boldsymbol{\frac{\partial}{\partial x}H_y - \frac{\partial}{\partial y}H_x = i\omega\varepsilon_0\varepsilon_r E_z} \quad (10)$$

The equations break into two groups describing, TE and TM modes, by substituting their definitions into the curl equations. Two differential equations, one for each polarization of light, are found. For a TE mode E_x is the only electric field component and the coupled DEs reduce to equation (12) describing it, as a function of x with $E_z = H_y = E_y = 0$. For a TM mode, H_x is the only magnetic field component and a similar DE is produced but instead for H_y, with $H_z = E_y = H_y = 0$. The nonzero field components can be calculated from relations derived from the curl equations.

$$\boldsymbol{E_y(x,z,t) = E_m(x)e^{i(\omega t - \beta z)}} \quad (11)$$

$$\boldsymbol{\left(\frac{\partial^2}{\partial x^2} + \frac{\partial^2}{\partial z^2} + k_0 n^2(x)\right)E_x(x,z,t) = 0} \quad (12)$$

$$E_m(x) = \begin{cases} C_2\, cos(\gamma_2 x) + C_3\, sin(\gamma_2 x)\,; & region\ 2 \\ C_1 e^{\gamma_1 x}; & region\ 1 \\ C_4 e^{-\gamma_3 (x-w)}; & region\ 3 \end{cases} \quad (13)$$

$$\gamma_1^2 = k_0^2 \left(\left(\frac{\beta}{k_0} \right)^2 - n_1^2 \right) \quad (14)$$

$$\gamma_2^2 = k_0^2 \left(n_2^2 - \left(\frac{\beta}{k_0} \right)^2 \right) \quad (15)$$

$$\gamma_3^2 = k_0^2 \left(\left(\frac{\beta}{k_0} \right)^2 - n_3^2 \right) \quad (16)$$

The solutions of equation (11) are either exponential or sinusoidal functions, depending on the sign of $(k_0 n)^2 - \beta^2$ which changes with x depending on the material in that region. This leads to solutions of the form in equation (13). The continuity of E and H at either side of the planar waveguide limits the number and shape of the bound modes that the structure can support. If the solution in region 2 is a decaying exponential, because of the choice of either ω or n, the only solution which satisfies the boundary conditions is 0 and therefore a bound mode is not supported. This strictly forces n_1 and n_3 to be less than n_2 for a mode to be bound in region 2, agreeing with the assertion from the total internal reflection model.

The boundary conditions at the discontinuities of the dielectric constant require the tangential magnetic and electric fields to be continuous. Since H_z is proportional to $\frac{d}{dy} E_x$, this is equivalent to forcing E_x to be smooth and continuous. Applying continuity of E_x and its derivative at the two boundaries gives four equations relating the solution amplitudes in the three regions and the propagation constant β. When these are solved, a relation between the thickness and propagation constant is found. This is solved numerically and the relation for TM modes is found by following the same procedure but solving for H_x instead of E_x. Equation (17) describes the dispersion relation for a TE mode and equation (18) represents the dispersion relation for a TM mode.

$$tan(\gamma_2 h) = \frac{\gamma_1 + \gamma_3}{\gamma_2 \left(1 - \frac{\gamma_1 \gamma_3}{\gamma_2^2} \right)} \quad (17)$$

$$tan(\gamma_2 h) = \frac{k(\overline{\gamma_1} + \overline{\gamma_3})}{\gamma_2^2 - \overline{\gamma_1 \gamma_3}} \quad (18)$$

With $$\overline{\gamma_i} = \frac{n_2^2}{n_i^2} \gamma_i \quad (19)$$

Three Dimensional Waveguide Structure, Marcatili Method

This analysis of waveguide modes can be extended into three dimensions using the Marcatili method. For TE mode bound in the structure described by Figure 3, E_y is zero and the curl equations can be arranged to express all the electric and magnetic field elements in terms of E_x. E_x is found to obey the two dimensional Helmholtz equation (24). Applying separation of variables leads to a solution in the five regions and applying boundary conditions at each of the four edges gives the mode confinement conditions. This analysis does not consider any field components in the hatched region of Figure 3.

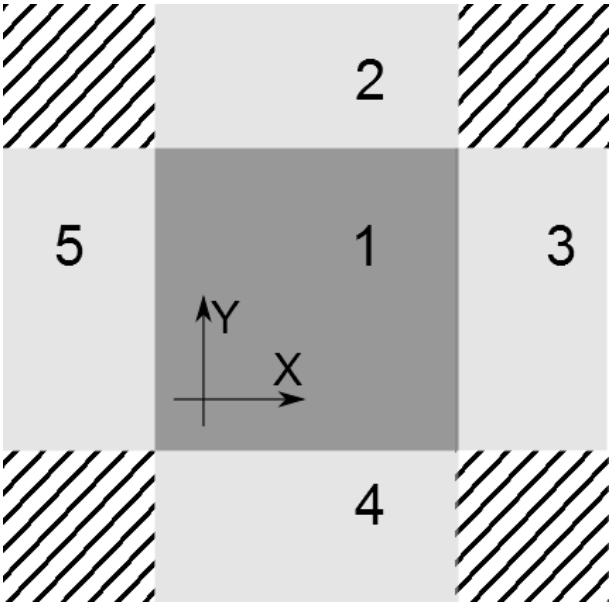

Figure 3: Diagram of Marcatili Method

The origin is in the centre of region 1, the high index region. Region 1 has a height of 2b and width of 2a.

$$H_y = \frac{1}{\omega\mu_0\beta}\frac{\partial^2}{\partial x \partial y}E_x \qquad (20)$$

$$H_z = \frac{1}{i\omega\mu_0}\frac{\partial}{\partial x}E_x \qquad (21)$$

$$H_x = \frac{1}{\omega\mu_0\beta}\left(\beta^2 E_x - \frac{\partial^2}{\partial y^2}E_x\right) \qquad (22)$$

$$E_Z = \frac{1}{i\beta}\frac{\partial E_x}{\partial y} \qquad (23)$$

$$\left[\frac{\partial^2}{\partial x^2} + \frac{\partial^2}{\partial y^2} + k_0^2\left(\varepsilon_r - \left(\frac{\beta}{k_0}\right)^2\right)\right]E_x = 0 \qquad (24)$$

$$E_x = \begin{cases} C_1 \cos(k_x x + \alpha_1)\cos(k_y y + \alpha_2);\ region\ 1 \\ C_2 \cos(k_x x + \alpha_1)\exp\left(-\gamma_y(y-b)\right);\ region\ 2 \\ C_3 \exp(-\gamma_x(x-a))\cos(k_y y + \alpha_2);\ region\ 3 \\ C_4 \cos(k_x x + \alpha_1)\exp\left(\gamma_y(y+b)\right);\ region\ 4 \\ C_5 \exp(\gamma_x(x+a))\cos(k_y y + \alpha_2);\ region\ 5 \end{cases} \qquad (25)$$

Imposing the boundary conditions at $y = \pm b$ yields a relation for k_y, and likewise the boundaries at $x = \pm a$ give a relation for k_x. These equations are solved numerically. It is interesting to note that the relation for k_y is the same as for that of a TE mode in a 3 layer waveguide and k_x is similarly related to the TM mode confinement relation. These two relations are described by equations (26) and (27) respectively. The final relation between k_x, k_y, β and, k_0 can be found by substituting the solution in region 1 into equation (24). This is the same relation as derived from the geometric ray treatment and is shown in equation (28). A similar set of steps can be taken to find the relation for a TM field. The unknown values in equation (25) can be found from the relations in the boundary conditions.

$$k_y b = \tan^{-1}\left(\frac{\gamma_y}{k_y}\right) + \frac{1}{2}(n-1)\pi \qquad (26)$$

$$k_x a = tan^{-1}\left(\frac{n_1^2}{n_2^2}\frac{\gamma_x}{k_x}\right) + \frac{1}{2}(M-1)\pi \quad (27)$$

$$k_x^2 + k_y^2 + \beta^2 = k_0^2 n_1^2 \quad (28)$$

Effective Index Method

The effective index method is the application of the separation of variables to equation (24). If we assume that the solution for E_x for a TE mode can be represented as a product of a function of only x and another function of only y then some simplifications to the differential equation can be made. When separating the PDE we first solve the separation constant as a function of x, equation (31), following from the previous study of three layer slab waveguide structure. This breaks the region into three regions, each a slab waveguide in the y direction, giving the separation constant as a function of x. The y dependence of the two dimensional PDE is then solved as a three layer TM mode, equation (32), in a similar way and the value of β is calculated.

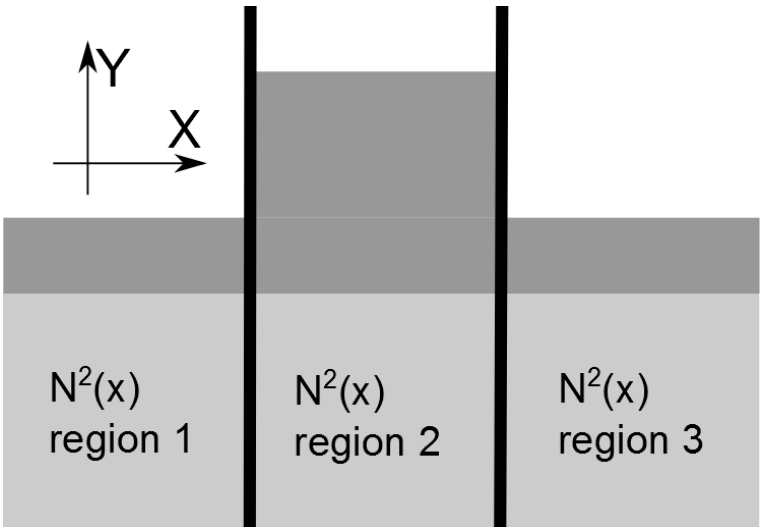

Figure 4: Diagram of effective index method

$$E_{x\ m,n} = X_m(x)Y_n(y) \quad (29)$$

$$\frac{1}{X}\frac{d^2X}{dx} + \frac{1}{Y}\frac{d^2Y}{dy^2} + k_0^2\left(\varepsilon(x,y) - \frac{\beta^2}{k_0^2}\right) = 0 \quad (30)$$

$$\frac{d^2Y}{dy^2} + k_0^2\Big(\varepsilon(x,y) - N^2(x)\Big)Y(y) = 0 \quad (31)$$

$$\frac{d^2X}{dx^2} + k_0^2\left(N^2(x) - \frac{\beta^2}{k_0^2}\right)X = 0 \quad (32)$$

This separation constant found in the first step of the method can be used to implement a 2D FDTD or beam propagation simulations of a 3D structure. This saves memory, thus allowing the simulation of larger, more complicated, devices. Two dimensional simulations predict the same phenomena (coupling, resonance, etc.) as their three dimensional counterparts do, but the results of the latter are more accurate. The simulations are performed by replacing the dielectric constant with the calculated

separation constant and then simulating a TM wave. We solve for a TM wave in the second step of the effective index method because the polarization of the electric field remains the same when the equation is separated. The electric field is perpendicular to the dielectric boundary, meaning that a TM mode is produced.

Solving for the propagation constants and mode structures of TM waves bound in Figure 4 using this method is handled as with the previous analysis but separating $\mathrm{H_x}$ instead. The separation constant is found using a TM three slab analysis and the propagation constant from a TE analysis using the separation constant.

2.2 Coupled Mode Theory

Basic Principles

Coupled mode theory is the application of perturbation theory to model the effects caused by changes in the dielectric constant's structure. It can predict resultant phenomena such as power exchange between modes of adjacent, or even the same, waveguide(s). The analysis is analogous to the time dependent perturbation of bound electrons by an external electromagnetic field, but in this case the perturbation appears in the dielectric constant instead of the potential function.

Assuming that the solutions, and the corresponding propagation constants, to the wave equation of the unperturbed structure are known we seek to find a solution to the DE with the addition of a z-varying perturbation of the dielectric constant. The solution can be approximated by equation (34), a sum of the solutions to unperturbed DE which satisfy equation (33). $E_m(x,y)$ is the x component of the electric field of the m^{th} TE mode. The amplitudes of the modes in the sum of the approximate solution are functions of the propagation direction and it is the evolution of these coefficients that describes the solution to the perturbed DE. When this approximation is substituted into equation (12), with equation (35) as the dielectric function, a set of equations describing the amplitudes of the modes, $A_m(z)$, is found. The relation is described by equation (36), after the slowly varying envelope approximation, equation (37), has been applied.

$$\left(\frac{\partial^2}{\partial x^2}+\frac{\partial^2}{\partial y^2}+\omega^2\mu_0\varepsilon_u(x,y)-\beta_m^2\right)E_m(x,y)=0 \qquad (33)$$

$$E(r)=\sum_m A_m(z)E_m(x,y)e^{-i\beta_m z} \qquad (34)$$

$$\varepsilon(r)=\varepsilon_u(x,y)+\Delta\varepsilon(r) \qquad (35)$$

$$-2i\sum_m \beta_m\frac{d}{dz}A_m(z)E_m(x,y)e^{-\beta_m z}=-\omega^2\mu_0\sum_n \Delta\varepsilon(r)A_n(z)E_n(x,y)e^{-i\beta_n z} \qquad (36)$$

$$\frac{d^2}{dz^2}A_m \ll \beta_m\frac{d}{dz}A_m \qquad (37)$$

We can then express the dielectric perturbation as a Fourier series in the z direction as in equation (38). This allows the inner product of the basis functions with the dielectric perturbation, to be used to further simplify equation (36), while adding an additional term to the phase mismatch element in the DE. Equation (39) describes the evolution of the mode amplitude coefficient functions after the

inner products of the m^{th} mode on the left is applied. In equation (39) m and n are summed over the modes in the analysis, a is summed over the Fourier components of the perturbation, and Λ is the periodicity of the perturbation.

$$\boldsymbol{\Delta\varepsilon(r) = \sum_{a} \Delta\varepsilon_a(x,y) e^{-ia\frac{2\pi}{\Lambda}z}} \quad \textbf{(38)}$$

$$\boldsymbol{\langle m|m\rangle \frac{d}{dz} A_m(z) = \frac{\omega^2\mu_0}{2i\beta_m} \sum_{n,a} \langle m|\Delta\varepsilon_a|n\rangle A_n(z) e^{i\left(\beta_m-\beta_n-a\frac{2\pi}{\Lambda}\right)z}} \quad \textbf{(39)}$$

$$\boldsymbol{\langle m|m\rangle = \int E_m^* \cdot E_m \, dxdy = \frac{2\omega\mu_0}{|\beta_m|}} \quad \textbf{(40)}$$

$$\boldsymbol{K_{m,n} = \frac{\omega}{4}\langle m|\Delta\varepsilon|n\rangle = \frac{\omega}{4}\int E_m^* \cdot \Delta\varepsilon E_n \, dx \, dy} \quad \textbf{(41)}$$

For a particular Fourier component of the perturbation the phase mismatch term, $\beta_k - \beta_n - a\,{}^{2\pi}/_{\Lambda}$, and the spatially dependent integral, $\langle m|\Delta\varepsilon_a|n\rangle$, determine the behaviour of the system. This integral's value describes the magnitude of the interaction between the fields of the two modes that exchange power, m and n, in the perturbation region, and is denoted by $K_{m,n}$, and in a two mode, level, system it is simply denoted K. Whenever the phase mismatch condition is not zero, the net coupling of one mode to the other is negligible. This is akin to conservation of energy in the analogy to the electron in an oscillating electric field. Off resonant solutions do exist but the change in amplitude of the solution functions, $A_m(z)$ is decreased. The power carried by each mode is proportional to the square of the amplitude.

Power couplers

To adapt this analysis to the power exchange between two modes of adjacent waveguides we treat the dielectric perturbation as the presence of a neighbouring identical waveguide and the second, coupled, mode as the mode in this neighbouring waveguide. Since the two modes that exchange power are identical, the phase mismatch term will be zero for the 0^{th} order Fourier component of the perturbation, i.e. a perturbation of a constant value such as the presence of an adjacent identical waveguide. A side view of a power coupler, with the perturbation region labelled, is shows in Figure 5.

Labelling the modes bound in the perturbation and original regions as numbers 2 and 1 respectively, the relation derived from equation (39) describing the evolution of the amplitude of mode 1 is given by equation (42). The overlap integral $\langle 1|\Delta\varepsilon_a|1\rangle$ is negated because the mode has a small magnitude in the perturbation region in comparison to the second overlap integral, $\langle 1|\Delta\varepsilon_a|2\rangle$, in the sum. The reverse view, changing the waveguide structure to be considered as the perturbation, yields equation (43) describing the evolution of the amplitude of mode 2. In equations (42) and (43), the 0^{th} Fourier component is used in the overlap integral to calculate K.

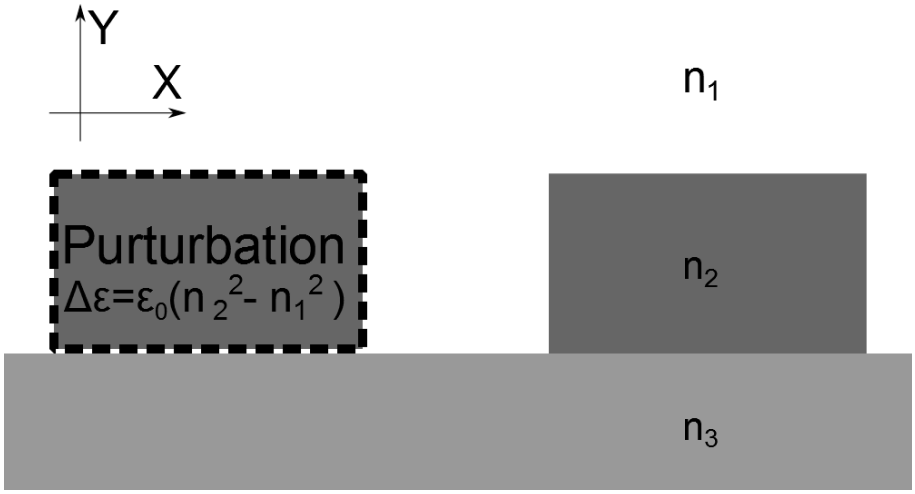

Figure 5: Side view of power coupler
Perturbation region in dashed area.

Uncoupling the system of differential equations is done by differentiating either one of equations (42) or (43) and substituting the result into the other. The solution to the phase matched DE are cosine and sine functions with angular frequency K, the overlap integral discussed above. For one mode initially excited at z = 0, the z-dependent solutions are given by equations (44) and (45):

$$\frac{d}{dz}A_1 = -iKA_2 \quad (42)$$

$$\frac{d}{dz}A_2 = -iK^*A_1 \quad (43)$$

$$A_1(z) = A_1(0)\cos(|K|z) \quad (44)$$

$$A_2(z) = -iA_1(0)\frac{K^*}{|K|}\sin(|K|z) \quad (45)$$

Adding a periodic structure to the waveguide can allow power to be transferred to a mode with a different propagation constant if the periodicity of the perturbation is chosen such that the phase matching condition is met.

Diffraction gratings

The addition of a periodic pattern to a waveguide (a diffraction grating) is employed in optical devices such as mode converters, Bragg reflectors, filters, and grating couplers. Their performance can be modelled using coupled mode theory.

A mode converter employs the phase matching condition to couple power between two modes in the same waveguide. Since the modes are orthogonal, power transfer between them is impossible without some form of perturbation. Power transfer is maximised when the phase matching condition is met and the overlap integral's magnitude and interacting length are correctly chosen. The two coupled modes are traveling in the same direction.

Bragg reflectors make use of the periodic perturbation to couple power between a forward traveling mode and the same mode propagating in the opposite direction. The periodicity can be chosen so that some wavelengths are allowed to pass through while others are reflected, creating a Bragg filter.

Periodic structures on the surface of a waveguide can also be used to couple power into and from an optical waveguide to a free wave. This will be discussed in the next section.

2.3 Coupling Power From a Free Space Wave into a Waveguide

Transferring optical power to and from a SOI chip cannot be accomplished by shining a laser at the waveguide. A ray incident on the surface of a 3-slab structure at any angle will simply refract through the high index medium and exit through the other side. A ray incident from the leading edge of the waveguide can excite a mode. This is called butt end coupling. Another common method used to excite modes in waveguide structures will be discussed below.

Grating Coupling

Placing a periodic perturbation on top of a waveguide structure can couple power out of the waveguide into radiative modes (free waves) which satisfy the phase matching condition. Since this analysis is completely linear the reverse process is also realizable - a grating coupling can couple power from free waves into modes of a waveguide. These grating couplings are easy to manufacture during an etching process and can be protected with an oxide layer to make the component more durable. In the case of a grating coupler (Figure 6) the periodic perturbation is obtained by removing a small portion of the dielectric from the surface of the waveguide.

Figure 6: Side view of grating coupler
Mode propagates in z direction

When relating a bound mode to a refracted incident free wave the propagation constant employed in the coupled mode equations is the z component of the wave vector, the same direction as the propagation of the excited mode, in the medium it is entering. The phase matching condition, equation (46), relates the periodicity of the perturbation to the propagation constant of the mode and the free space wavelength. $\beta_0$is the propagation constant of the bound mode and $k_z = n_1 k_0 \sin(\theta_i)$ is the z component of the free wave vector if it were to refract without the presence of the perturbation. θ is the refracted angle of the free wave.

$$\boldsymbol{\beta_0 - k_z - \frac{a2\pi}{\Lambda} = 0} \quad (46)$$

These structures can be designed to operate over large wavelength ranges. They are designed for maximal coupling at a specific frequency and input angle, usually 10° to avoid crowding. The chips used in these experiments all used grating couplings to transfer optical power to and from the laser and optical power sensor.

2.4 Numerical Simulations

The algebraic models developed so far are useful for understanding the behaviour of basic structures used in the field of photonics, but ultimately the relations represent idealized cases of the device layout. Couplers, for example, do not have a well-defined interaction length. For example, as the waveguides are brought into proximity with one another the overlap integral K will change. A first principles simulation of the spectral response of these structures is therefore a useful tool in fine-tuning their performance.

Beam propagation

Beam propagation simulations are a powerful tool for predicting power outputs of waveguide structures as well as power coupling between modes [3]. They can also be adapted to accurately calculate the propagation constants and mode structure of complex waveguides. Similar to coupled mode theory, we start with the assumption that the z and t dependence of the electric field are known and factored out, as well as that the second derivative of u, the envelope function, with respect to z is negligible compared to the first.

$$\boldsymbol{E(r,t) = u(r)e^{iwt-i\beta z}} \quad (47)$$

$$\boldsymbol{\frac{\partial u}{\partial z} = \frac{-i}{2\beta}\left(\frac{\partial^2}{\partial x^2} + \frac{\partial^2}{\partial y^2} + (n^2(x,y,z)k^2 - \beta^2)\right)u(r)} \quad (48)$$

If $u(r, z = 0)$ is a mode of the waveguide structure (so that equation (48) is zero for the waveguide cross-section) then this simulation will track the amplitude of the mode as it progresses down a waveguide structure. The value of k_n, which depends on the index of refraction, will change for each z segment of the numerical integrator, depending on the nature of the waveguide structure being simulated. Simple applications of this method accurately predict the power exchange between waveguides but do not yield accurate results for devices, like resonators, which change direction significantly, unless higher order methods are employed.

The beam propagation method can be adapted to calculate mode structures and propagation constants. This is an important tool because the numerical scheme does not revolve around root finding and can be used on any arbitrarily complex waveguide geometry.

Summary of BEAMPROP Mode Calculation Numerical Method:

Step 1 Initialize electric field with arbitrary distribution. When this initial distribution is decomposed into the modes of the waveguide, equation (49), the initial excitation of the waveguide must include the mode that you wish to study.

Step 2 Using equation (48), evolve the electric field in the negative idz direction. The mode with the largest propagation constant will increase the most in this step.

Step 3 The electric field is normalized and equation (50) is used to calculate the current approximation of the propagation constant.

Step 4 Test for tolerance of change in propagation constant. If condition is not met, return to step 2. p, in equation (50), is the output electric field distribution of the iteratively evolved and normalized process.

$$\boldsymbol{E}(\boldsymbol{x},\boldsymbol{y},\boldsymbol{z}) = \sum \boldsymbol{c_m u_m}(\boldsymbol{x},\boldsymbol{y})\, \boldsymbol{e}^{-i\boldsymbol{\beta} z} \quad \textbf{(49)}$$

$$\boldsymbol{\beta_p} = \int \left(\boldsymbol{p}^* \left(\frac{\boldsymbol{d^2 p}}{\boldsymbol{dx^2}} + \frac{\boldsymbol{d^2 p}}{\boldsymbol{dy^2}} + \boldsymbol{k^2 p} \right) \right) \boldsymbol{dx\, dy} \Big/ \int \left(\boldsymbol{p_m^* p_m} \right) \boldsymbol{dx\, dy} \quad \textbf{(50)}$$

Propagating a mode in the imaginary z direction (as opposed to the real z direction), will cause a change in amplitude (instead of phase) related to the propagation constant. Since the equations describing mode propagation are linear, any superposition of modes will evolve independent of one another. If some superposition of modes, say a Gaussian profile, is propagated in the negative imaginary direction ($-idz$), using a numerical integrator, the mode with the largest propagation constant will grow the most. If then at every step in the integration the optical power is normalized, the steady state solution of this iterative procedure will be the bound mode of the waveguide structure with the largest propagation constant. The propagation constant can be calculated by using inner products of the Helmholtz equation shown in equation (50). The approximate value of β calculated at each step is used by equation (48) to evolve the field at each step in the integration.

Forward Difference Time Domain (FDTD)

A first principles simulation of Maxwell's equations can be realized by employing the two curl relationships. The spatial derivatives of the magnetic and electric fields provide the temporal evolution of the electric and magnetic fields, respectively. To initiate a continuous wave FDTD simulation, the mode structure and propagation constant must be known ahead of time as they are crucial to the boundary values on the edge where the wave is incident.

This type of simulation can incorporate structures of any geometry and light pulses of any polarization. Use of FDTD simulations for resonator structures is instructive as resonator structures require the formation of standing waves in the ring structure which take the light pulse multiple trips around the resonator to form. The output of a one wavelength simulation of a ring structure is shown in Figure 7

The main drawback of this method is that it is very memory intensive. Using the Crank Nicholson method, a three dimensional simulation requires inverting a $3N^3\ by\ 3N^3$ matrix (where N is the number of simulated points). For large choices of N this becomes difficult. Crank-Nicholson integrators are typically used as a numerical technique because of their long-term stability.

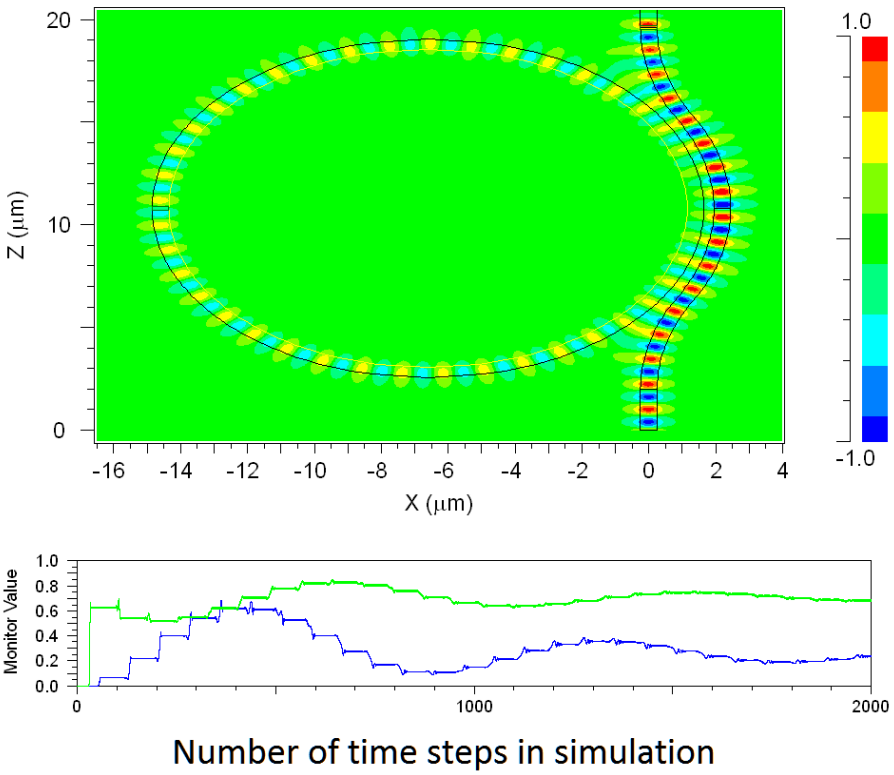

Figure 7: 3D FDTD simulation of resonator structure.
The two monitor values show the transmitted power in green and the circulated power in the ring structure in blue. The simulation was run with a continuous wave input until the steady state solution was reached. 3D ring resonator structure with strip waveguide. Height 300 nm, width 500 nm.

FDTD continuous wave simulations can be repeated for a spectrum of input wavelengths, provided that their corresponding mode structures have been approximated beforehand. The spectral response of the structure is found by plotting the transmitted power vs the input wavelength from each simulation. This structure geometry was present on one of the chips, but was not used as a sensor. This simulation was used to study the change in coupling coefficient, causing a change in peak shape, as the cover index of refraction was changed.

Boundary Conditions

Boundary conditions are required to generate a unique solution of any differential equation. When considering waveguide structures in reality any power that escapes from a waveguide will propagate unhindered as it travels outside the simulation volume. In a computer simulation, the boundary conditions in the simulation must allow this to happen so that these stray rays do not interfere in any way with the data collected. Simply forcing the boundary to a constant value generates reflected rays and is undesirable as these rays affect power measurements. Continuous boundary conditions, allowing rays that exit one edge of the simulation to re-enter from the opposite side, are undesirable for the same reason.

One way to mimic the natural behaviour of light rays radiating out of the simulation area is to simulate an absorbing medium on the boundary of the simulation volume. This will dissipate power from these

rays and minimise their interaction with the simulation. This can be undesirable for simulations of larger structures because of the added computational memory required by the insulating volume.

Transparent boundary conditions are another way to mitigate the effects of stray waves on FDTD simulations. The idea behind this method is to dynamically change the boundary values to mimic any outgoing rays, allowing them to “pass outside” the simulation volume. This method uses less memory than simply including an absorbing area in the simulation.

3 Passive Optical Structures

3.1 Common Passive Optical Structures

Now that some background of propagation of modes in optical waveguides has been presented, a brief summary of some optical component of interest to sensor applications will be presented. In the field of optical communication, multiplexing and de-multiplexing is of crucial importance to the efficient transfer of data. Multiplexing is the process of adding a signal, modulated on a particular wavelength, to an existing EM wave, de-multiplexing is the process of removing a modulated signal from an EM wave. When analysing multiplexed signals in a linear medium, each wavelength must be analysed separately.

Most passive optical devices can be modelled using the relations discussed earlier. While active optical devices (which make use of imbedded electrical components such as heaters or electrically active materials to tune devices' spectral response) exist, this thesis focuses solely on passive devices and their sensor applications. To better analyse how passive devices (and large arrangements of them) behave it is convenient to represent the evolution of the modal field distributions in the device as matrix equations. This allows light propagation through a series of devices to be modelled by the multiplication, on the left, of the corresponding matrix representation of each passive waveguide component to the input power.

Power splitter

The device described in Figure 8 is a power splitter. It can divide power from one input to both outputs. The spectral response of this device's output ports is accurately modelled by coupled mode theory.

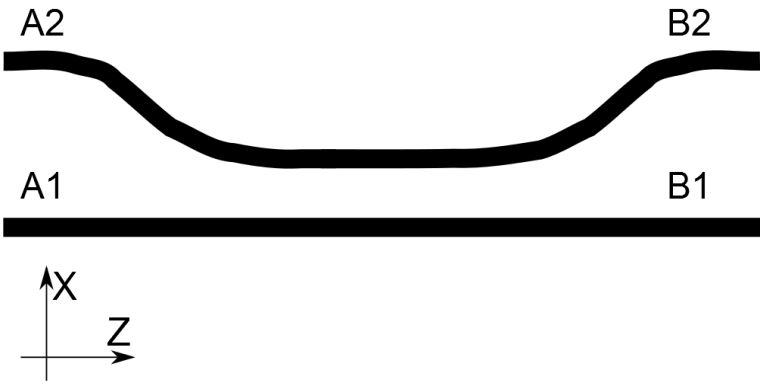

Figure 8: Diagram of Power splitter

From the solution of coupled mode amplitude for adjacent waveguides, equations (44) and (45), the complex amplitude inputs, A_1 and A_2, are related to the outputs, B_1 and B_2, over an interaction length L by equation (51), assuming that both waveguides are identical.

$$\begin{bmatrix} \boldsymbol{B_1} \\ \boldsymbol{B_2} \end{bmatrix} = \begin{bmatrix} \boldsymbol{cos}(|\boldsymbol{K}|\boldsymbol{L}) & \boldsymbol{i\,sin}(|\boldsymbol{K}|\boldsymbol{L}) \\ \boldsymbol{i\,sin}(|\boldsymbol{K}|\boldsymbol{L}) & \boldsymbol{cos}(|\boldsymbol{K}|\boldsymbol{L}) \end{bmatrix} \begin{bmatrix} \boldsymbol{A_1} \\ \boldsymbol{A_2} \end{bmatrix} \quad \textbf{(51)}$$

The overlap integral K does not experience a great deal of spectral dependence. When being used as a power splitter, the interaction length L is chosen so that $KL = (n + 1/2)\,\pi/2$ forcing all the elements in the transfer matrix to have magnitude $1/\sqrt{2}$. An input wave at A_1 with magnitude 1 will produce two output waves, each with magnitude $1/\sqrt{2}$. The power carried by the waves at B_1 and B_2, proportional to the square of the amplitude, each have a value of $1/2$. This same choice of L will also evenly divide power from path A_2 among the outputs. This is a 50/50 power splitter.

Mach-Zehnder Interferometer

From a power splitter and two isolated waveguides of different lengths we can create an interference pattern. Using the known z dependence of isolated modes, the propagation constant, the matrix describing the evolution of non-interacting identical modes over different distances is given by equation (52).

$$\begin{bmatrix} \boldsymbol{B_3} \\ \boldsymbol{B_4} \end{bmatrix} = \begin{bmatrix} \boldsymbol{e^{-i\beta L_1}} & \boldsymbol{0} \\ \boldsymbol{0} & \boldsymbol{e^{-i\beta L_2}} \end{bmatrix} \begin{bmatrix} \boldsymbol{B_1} \\ \boldsymbol{B_2} \end{bmatrix} \quad (52)$$

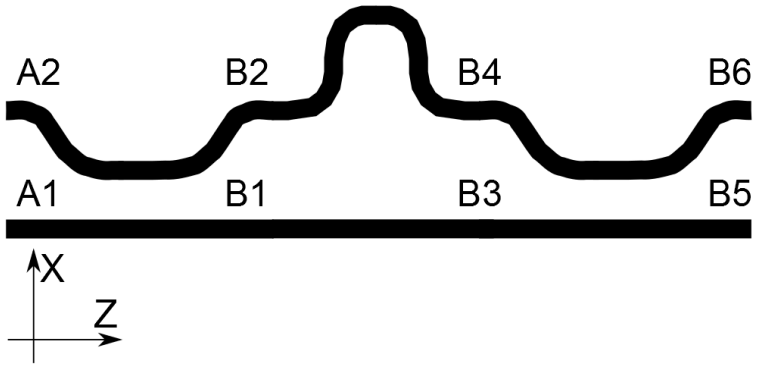

Figure 9: Diagram of Mach-Zehnder Interferometer

The full matrix expression of the device in Figure 9 is given by equation (53). Both power splitters used in this equation were 50/50. When solving for a single excitation from port A_1, the solutions for ports B_1 and B_2 are given in equations (54) and (55). taken from [4].

$$\begin{bmatrix} \boldsymbol{B_5} \\ \boldsymbol{B_6} \end{bmatrix} = \begin{bmatrix} \boldsymbol{1/\sqrt{2}} & \boldsymbol{i1/\sqrt{2}} \\ \boldsymbol{i1/\sqrt{2}} & \boldsymbol{1/\sqrt{2}} \end{bmatrix} \begin{bmatrix} \boldsymbol{e^{-i\beta L_1}} & \boldsymbol{0} \\ \boldsymbol{0} & \boldsymbol{e^{-i\beta L_2}} \end{bmatrix} \begin{bmatrix} \boldsymbol{1/\sqrt{2}} & \boldsymbol{i1/\sqrt{2}} \\ \boldsymbol{i1/\sqrt{2}} & \boldsymbol{1/\sqrt{2}} \end{bmatrix} \begin{bmatrix} \boldsymbol{A_1} \\ \boldsymbol{A_2} \end{bmatrix} \quad (53)$$

$$\left|\frac{\boldsymbol{B_5}}{\boldsymbol{A_1}}\right|^2 = \frac{\boldsymbol{1}}{\boldsymbol{2}}\left(\boldsymbol{1} - \boldsymbol{cos}\left(\boldsymbol{\beta}(\boldsymbol{L_a} - \boldsymbol{L_b})\right)\right) \quad (54)$$

$$\left|\frac{\boldsymbol{B_6}}{\boldsymbol{A_1}}\right|^2 = \frac{\boldsymbol{1}}{\boldsymbol{2}}\left(\boldsymbol{1} + \boldsymbol{cos}\left(\boldsymbol{\beta}(\boldsymbol{L_a} - \boldsymbol{L_b})\right)\right) \quad (55)$$

This structure exploits a path length difference to achieve spectral response from the input. This design can be used to split two signals carried on two wavelength bands. If the path difference is chosen so that $\beta_1(L_a - L_b) = (2m + 1)\pi$ and $\beta_2(L_a - L_b) = 2n\pi$, then any signal composed of these two modes incident on port A_1 will be split to ports B_1 and B_2 respectively. This structure can also be used

to add two signals, one carried on wavelength β_1 at port A_1 the other with β_2 at port A_2. If $\beta_1(L_a - L_b) = (2m+1)\pi$ and $\beta_2(L_a - L_b) = (2n+1)\pi$ then both signals will be output on port B_1. These structures are popular for sensing strain because the long path length lends itself to high sensitivity of the measurand [5] [6].

If one of the paths of the interferometer is open to changes in the environment then any effects on β of this path will be reflected in the transmitted power. Influences such as temperature changes, stress, and changes to the guiding structure of the sensing arm of the interferometer would affect the transmitted power. Modelling and characterization of the environmental effects allow the device to be used as a sensor. This will be discussed more with the ring resonator structure studied and tested in this thesis.

Ring Resonators

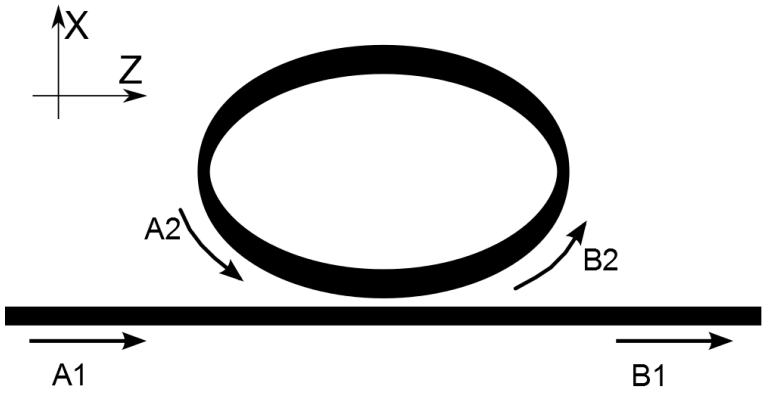

Figure 10: Diagram of ring resonator

Resonator structures can be created from a power coupler by connecting the second output of the coupler to its second input. A pictorial representation of a ring resonator is given in Figure 10. This creates two separate waveguide pathways which interact in a small region, described by the power coupler. The length of the closed waveguide (referred to as a ring or racetrack), is the critical factor in this device's frequency response. The change in amplitude per round trip in the ring is $\alpha = e^{-iaL}$ with a being the complex component of the medium's refractive index.

A coupler structure has a more general representation. Defining the coupling and the through coupling coefficients as $t = \cos(KL)$ and $k = \sin(KL)$, respectively, gives the matrix relation for a power coupler in the form of equation (56) for an arbitrary interaction of length L. The solution for the through power of the resonator structure is described by equation (58), using equation (57) to relate the field amplitude at B_2 and A_2. Studying the transmittance relation on resonance, when the phase $\beta L = 2m\pi$, the critical coupling condition is found by plotting the equation (58) as a function of t for a fixed value of α. A plot of the on resonance transmission for α=0.95 is given in Figure 11. When $t = \alpha$, the field amplitude at port B_1 on resonance is zero.

$$\begin{bmatrix} \boldsymbol{B_1} \\ \boldsymbol{B_2} \end{bmatrix} = \begin{bmatrix} \boldsymbol{t} & \boldsymbol{ik} \\ \boldsymbol{ik} & \boldsymbol{t} \end{bmatrix} \begin{bmatrix} \boldsymbol{A_1} \\ \boldsymbol{A_2} \end{bmatrix} \quad \textbf{(56)}$$

$$\boldsymbol{A_2 = \alpha e^{-i\beta L} B_2} \quad \textbf{(57)}$$

$$\left|\frac{B_1}{A_1}\right|^2 = \frac{\alpha^2 + t^2 - 2\alpha t\, cos(\beta L)}{1 + \alpha^2 t^2 - 2\alpha t\, cos(\beta L)} \quad (58)$$

The variables α and t, and hence k, affect the nature of the resonator transmission spectrum. The round trip loss coefficient decreases as the length of the resonator increases. The radius of curvature of the curves in the structure also affects the round trip loss, as smaller radius bends have lower transmitted power. The coupling coefficient can be approximated by numerically evaluating an overlap integral in the perturbation region as well as controlling the interaction length. In the algebraic model of the resonator structure, there was no way to account for non-constant coupling parameters during the interaction length of the power splitter. More accurate resonator transmission simulations come from FDTD programs as detailed later in this section.

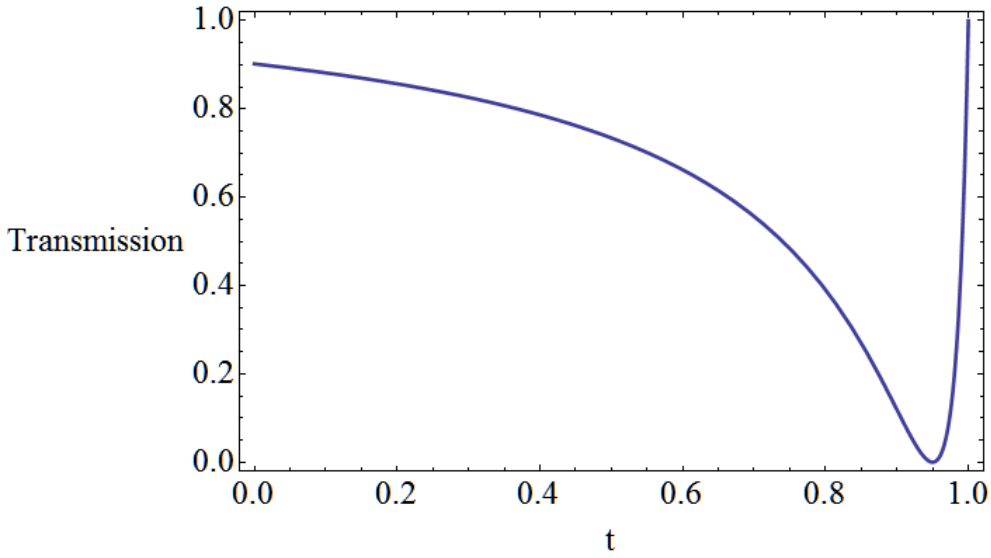

Figure 11: On resonance transmittance
Relative output power as a function of coupling t value. Round trip loss $\alpha = 0.95$.

Studying the off-resonant equation shows the possible peak shapes that this structure is capable of producing. For a resonator designed such that $\alpha = t$, increasing t (and hence α) increases the narrowness of the resonance peaks. The plots in Figure 12 show various spectral responses a resonator structure is capable of producing. Resonators with narrow peaks (high finesse), have very low loss and large t values.

Apart from the location of a resonance peak, the distance between peaks (the free spectral range or FSR) is also a characteristic of the resonator structure. This is not a constant value, but rather it changes depending on the wavelength range used, though the value does not vary greatly from peak to peak. For a resonator of length L a resonant wavelength produces a propagation constant that satisfies equation (59). Assuming that the effective index is constant between peaks, the propagation constant follows equation (60) and , the FSR of a resonator is described by equation (61).

$$\beta_1 L = 2m\pi \quad (59)$$

$$\beta = {}^{2\pi n_{eff}}/_{\lambda} \quad (60)$$

$$FSR = \lambda^2 / n_{eff} L \quad (61)$$

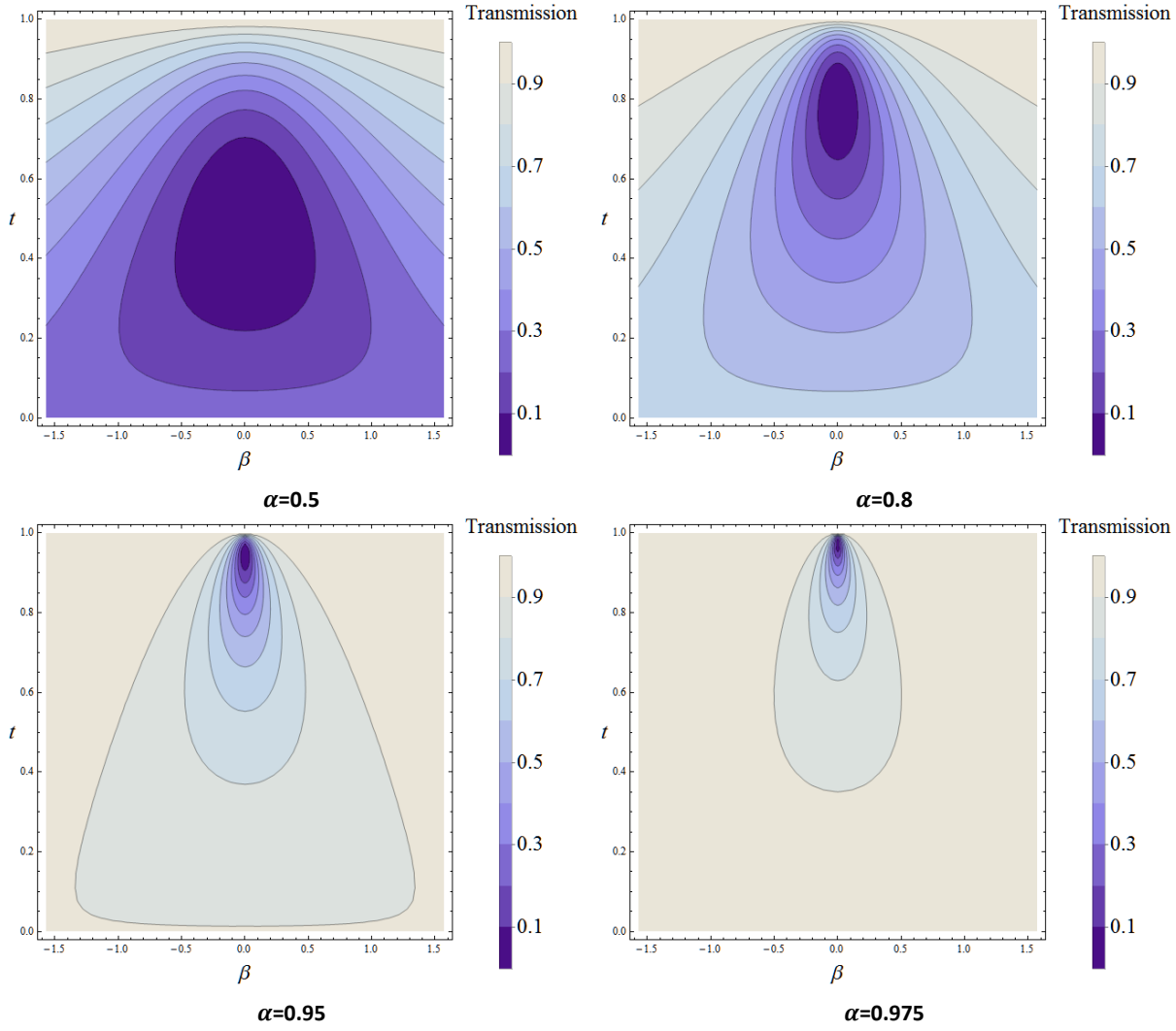

Figure 12: Resonator peak shape

Relative power output as a function of propagation constant and coupling coefficient t. For various loss values

This structure's performance can be further refined by placing a power coupler on the ring structure opposite the first resonator or by coupling two resonators together. Both designs are shown in Figure 13. Placing a coupler that only takes away a small portion of the power in the ring will create a structure that behaves as a wavelength selective switch. The circulating power of a resonator, the power trapped in the ring of the device described in Figure 10, is given by equation (62). This function experiences a maximum when the through power of the resonator, equation (58), is at a minimum. Adding another waveguide near the ring, as in the left side of Figure 13, allows some of the circulating power to exit the ring. The resonator can be designed to remove a specific wavelength from the incoming signal at port A1 while leaving other wavelengths unaffected. The time reversal of these passive structures allows this to be adapted to add a signal carried on a wavelength to an existing input.

Multiple rings placed in series increases the FSR of the device drastically through the Vernier effect. The FSR of a resonator is proportional to the path length. The series arrangement allows devices with small footprints to achieve spectral responses normally reserved for larger devices

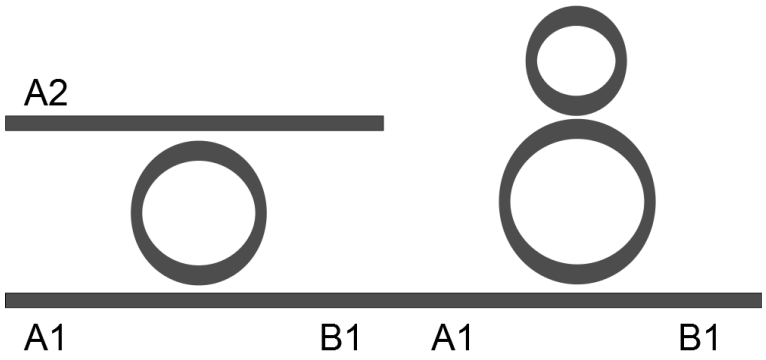

Figure 13: Resonator structures
Structure on the left measures circulating power in resonator. Structure on the right exploits Vernier effect to achieve large FSR.

$$\left|\frac{\mathbf{B_2}}{\mathbf{A_1}}\right|^2 = \frac{\boldsymbol{\alpha^2(1-t^2)}}{\mathbf{1+\alpha^2 t^2 - 2\alpha t\cos(\beta L)}} \quad \textbf{(62)}$$

3.2 Sensing Devices

Optical sensors employ changes in transmission properties caused by environmental effects, measured against some baseline value, to deduce the value of an environmental property. When mathematically modelling a sensing device the property that the sensor is measuring is called the measurand. The sensor tracks observable changes in either relative power transmission at a fixed wavelength or a broad spectrum sweep to infer the value of the measurand. The passive optical device models presented above are sufficient to model the performance of sensing devices. The sensitivity of a sensor is defined as the change in the measured output divided by the corresponding change in measurand [7].

The sensor structure tested in this thesis is simplistic, a single ring resonator partially exposed to the air, but is a good proof of concept for the viability of the SOI platform for sensors. A two ring resonator structure exploited the Vernier effect to achieve a sensitivity of 1300 nm/RIU. A resonator-interferometer structure achieved sensitivity of $1000\,\mu m/RIU$ [8], another compound structure reported a sensitivity of $688.3\,nm/RIU$ [9]. More complex phenomena can also be studied using SOI chips, a surface plasmon MZI sensor reported a sensitivity of 102 nm/RIU over a small active sensing region [10]. Exotic waveguide structures experience increased sensitivity to changes in refractive index, a study of a slot waveguide resonator structure yielded a sensor with sensitivity of 300 nm/RIU [11]. A whispering gallery mode resonator tested in [12] achieved a sensitivity of $120\,nm/RIU$. Photonic crystal structures are highly sensitive to changes in the surrounding index of refraction [13] [14] [15].

Types of Sensors

Attenuation

As discussed before, part of the EM field of any bound mode exists outside the high index area of a waveguide. This evanescent field will interact with the material that surrounds the waveguide. Figure 14 is a simple diagram of such a sensor. An attenuation sensor can be described as a power source

leading to a power splitter and two paths, each ending in an optical power meter. One path, the reference arm, is isolated from changes in the measurand while the other path, the sensing arm, is not. If the interaction of the measurand on the sensing arm affects the attenuation of the mode then the change in output power of the sensing arm, relative to the reference arm, is an indicator for change in the measurand. For example, if the sensing arm has a break in it and is unsupported then a slight change in alignment of this break would result in a change in transmitted power. One example of an application of this type of sensor is in accelerometers, where the displacement of the sensing arm is proportional to the acceleration of the chip by Hooke's Law.

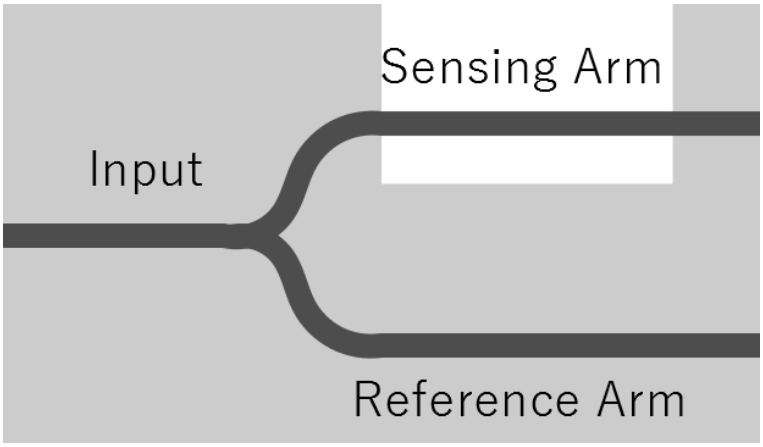

Figure 14: Basic Single Frequency Sensor Diagram.

Attenuation in waveguides can also be modified by increasing bending along the path. A pressure sensor can be realized by placing a fibre in between an interlocking pattern so that as the interlocking pattern is compressed bends in the fibre become more pronounced. Increasing pressure increases the bending loss of the fibre, making the changes in output power an indication of pressure. In [16], bending loss was measured in an array of fibres to map applied pressure. Chemical coatings are used to change the loss in an optical waveguide, and indicate changes in gas concentration [17].

Phase

The phase difference exploited in the transfer function of an MZ interferometer (see Figure 9) is $\Phi = \beta_1 L_1 - \beta_2 L_2$. With path one as a reference, L_1 and β_1 being constant, any changes in either β_2 or L_2 will affect the output power. Sensors that make use of phase measurements have periodic transmittance functions and thus possess a limited rage of operation dictated by the sensitivity. If a wavelength is chosen so that no power is transmitted, (i.e. equation (54) is zero), then the measurand can only affect the product $\beta_2 L_2$ by a maximum shift of π in either direction without generating an ambiguous reading.

The MZ interferometer can be designed to measure stress. If the sensing arm stretches for a large distance in one direction then any changes in length caused by applied stress in that direction would affect the transmission power. While an applied stress in the perpendicular direction will also change the transmission power, this effect is small compared to a stress applied parallel to the sensing arm.

Wavelength

Sensors can utilize a spectrum of light to determine the location of a transmission feature and track its location with changes to the measurand. Resonator structures are examples of wavelength modulated sensors and will be explored in detail.

All types of sensors operate according to Figure 15. The form of $F(x, \beta)$, the transfer function of the sensing structure, includes any dependence on the measurand x. The way the measurand affects the modes supported in the waveguide can be used as an indicator of changes in the measurand. Measuring changes in transmitted power due to variable loss is an example of a way changes in mode can indicate changes in the measurand. This relation is described by the function $\beta(x, \lambda)$. Using mode calculation techniques coupled with the passive waveguide structure analysis discussed above, a mathematical description of a sensor's expected output and sensitivity can be studied.

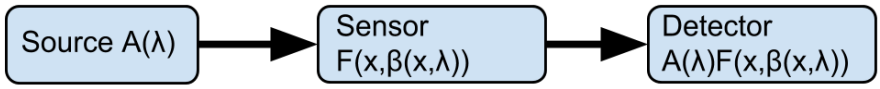

Figure 15: Pictorial Representation of a Sensor

Sensors that make use of a single frequency light source have their dimensions and the frequency of light chosen so that any variations in transmission power with respect to the measurand are maximised, maximising sensitivity. Any periodicity in the transmission spectrum must be accounted for as it will limit the active sensing range of the device.

One way to tune these devices is to limit the interaction area over which the measurand can affect the device. If the interaction of the measurand is limited to a portion of the path, l, then phase accumulated in the sensing arm of an MZ interferometer is replaced by $\beta_1(L_2 - l) + \beta_2 l$, decreasing sensitivity but increasing active sensing range. In a similar way, the changes that a measurand causes in the propagation constant can be controlled by waveguide geometry choices such as the thickness of the waveguide cover. Since these modifications to the waveguide in the manufacturing step are not entirely precise, it is best to calibrate such sensors rather than use the simulated values.

Thermally tuned devices can also be manufactured and are often used in industry. These chips have a resistor buried near the waveguide with connected copper contacts placed elsewhere on the chip. When a voltage between the contacts is applied, the power dissipated by the resistor as heat causes the chip to expand, in turn causing a change in path length for any optical device near this buried resistor. These components are used in the operation of tuneable communication devices such as filters and switches. In order to maximise performance, they are calibrated and then kept in thermal isolation. Fine tuning of a device's spectral response is possible after the manufacturing step [18].

A wavelength dependent sensor requires a tuneable light source. Further, the measurand value should not vary significantly over the period of time required to accurately sample the transmission spectrum of the sensor. In some cases this is acceptable but for other measurands, such as acceleration, the value can change too quickly to make swept measurements meaningful. The algebraic sensitivity analysis of wavelength dependent sensors, such as the resonator structure, is performed by tracking the values of constant phase, $\beta L = 2M\pi$, as the measurand is varied. Since the path length is constant the behaviour

of the indicator, the wavelength required to generate a resonance peak, is dictated by the dispersion relation $\beta(x, \lambda)$.

Sensitivity Calculations

For a single wavelength sensor, the measured output is a ratio of optical powers from the sensing and reference arms of the device. The measured output for a wavelength dependent sensor is the wavelength of a defining feature of the device's transmission spectrum, such as a resonance peak. Predicting the sensitivity of a sensor is done by differentiating the measured output with respect to the measurand. This derivative is the predicted sensitivity. Sensors are optimized before manufacture to maximise this value by changing device dimensions, input wavelength and waveguide geometry. The uncertainty of a sensor is the variance in the predicted output. It is determined by the accuracy with which the measured output can be determined as well as any uncertainty in the modelled relation used to determine the measurand value.

4 Theoretical Results

The device considered for the remainder of this thesis is a high-finesse ring resonator, with half of the ring path open to the air. Fluids with different refractive indices placed on the surface of a chip affect the bound modes of the guiding structure, changing the overall phase accumulated in the exposed portion of the ring. By tracking the shift in wavelength required to generate a transmission peak with a frequency swept laser, the index of refraction of the material covering the resonator can be calculated.

By calculating the propagation constant using numerical approximations and then using the resultant model in the passive waveguide structures discussed previously, we seek to predict the direction and magnitude of the shifts in resonance peak of a resonator due to changes in mode structure. Assuming that the sensing experiments will take place in thermal isolation, so that the length of the resonator is constant, the only effect on the transmission peaks will come from changes in propagation constant. High precision index matching fluids can be used to calibrate the sensor and test the computer models' accuracy.

4.1 Mode Calculation

In this section we will investigate how waveguide geometry, waveguide cover index, and spectrum of wavelengths affect the propagation constant of the modes supported by waveguide structures. The method by which the peak location and FSR is calculated from simulation outputs is the same for every type of simulation.

Given a particular waveguide geometry, cover index of refraction, and free space wavelength each model can be numerically solved for a predicted propagation constant. Multiple runs of these simulation with varied parameters can generate data points that are used to create a 3D interpolating function. This is used to predict the relation β has on the free space wavelength and the cover index of refraction. In a resonator, the peak location shift is determined by level sets of the interpolating function. Since the resonator structure can be made to have an arbitrary length, any β could be a resonance peak and so the particular value of β used in this analysis is inconsequential, as long as it is a value supported by a bound mode in the structure.

The change in FSR can also be quantified with the interpolating function. Two adjacent resonance peaks can be found by choosing a path length L and two values, β_1 and β_2, on the dispersion relation that satisfy $\beta_1 L - \beta_2 L = 2\pi$. Repeating the process described above for both these β values yields the predicted change in FSR.

Three Layer Slab

The determination of the propagation constant and EM field structure of TE modes in a three layer slab waveguide can be reduced to solving equation (17) numerically for β. For convenience equation (17) is shown again below as equation (63). Because n_2 is greater than n_1 and n_3 the square of β must be greater than the largest of $k_0 n_1^2$ and $k_0 n_3^2$ as well as less than $k_0 n_2^2$.

$$\boldsymbol{\tan(\gamma_2 h) = \frac{\gamma_1 + \gamma_3}{\gamma_2\left(1 - \frac{\gamma_1\gamma_3}{\gamma_2^2}\right)}} \qquad \textbf{(63)}$$

γ_1, γ_2 and γ_3 from equations (14), (15), and (16) all depend on β, the free space wavelength, and the corresponding index of refraction. The left hand side of equation (63) depends on the thickness of the slab, and increasing h increases the number of periods of the tangent function that will appear in a plot versus β, thereby increasing the number of bound modes supported by the structure.

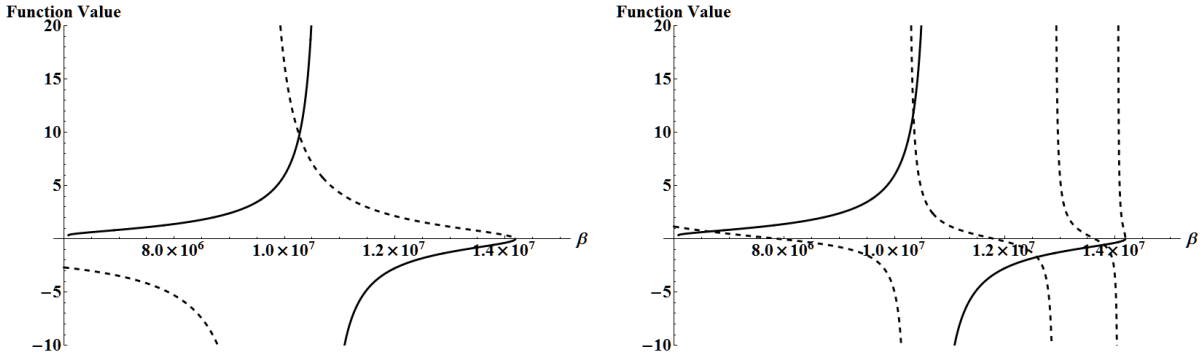

Figure 16: Three layer slab confinement condition

Plots of equations on left (dashed) and right (undashed) hand side of equation (63). Intersection of these curves are propagation constants of bound modes. Cover index of refection 1.5, core index of refraction 3.5.

The right hand side of equation (63) has a discontinuity over the region of accepted values of β. The intersection of the functions on the left and right of equation (63) is calculated numerically and these intersections describe the even and odd solutions. Plots of the confinement relation are shown in Figure 16 for two slab waveguides of different thicknesses. The values of the index of refraction were 1.5 for the top and bottom layer and 3.5 for the middle layer. The unknown coefficients of the electric field function can be found using algebraic relations at the boundary.

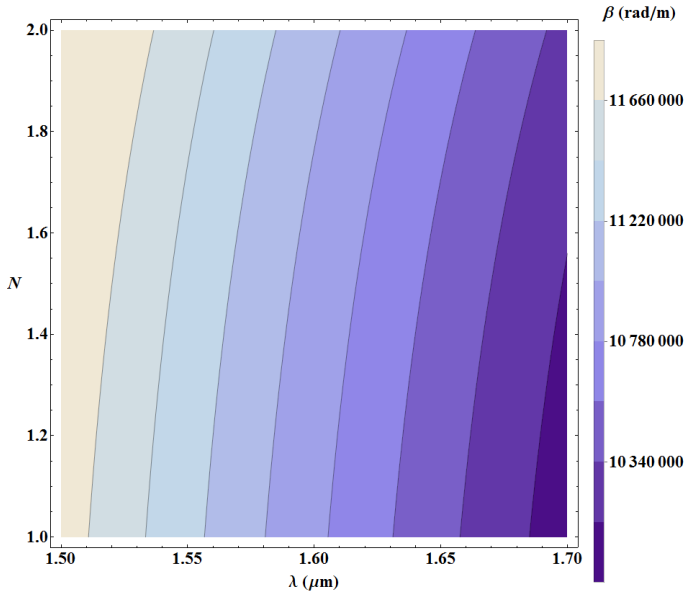

Figure 17: Three layer slab simulated propagation constant

Propagation constant vs cover index of refraction and wavelength. 200nm thickness. SiO2, Si, vacuum layers

Figure 17 shows a contour plot of a three slab propagation constant simulation with varied cover index of refraction and wavelength. The contour lines of this plot track the wavelength required to produce a

resonance peak for a cover index of refraction N. The three slab simulation indicates that the resonance peaks will shift upwards as the cover index of refraction is increased. The sensitivity analysis of a ring device using simulation data will be performed later.

Beam Propagation Mode Calculation

Rsoft is a software package which includes beam propagation simulation tools that can be employed to determine the modal field patterns and propagation constants of arbitrary optical waveguides. The software package provides an environment for point-and-click layout of waveguide structures in the CAD software as well as allowing for series of simulations with varied parameters such as free space wavelength and material properties or changes in the geometry of the waveguide. This allows the user to simulate how changes in design parameters or the measurand will affect the spectral response of a passive waveguide structure. This is particularly useful because the beam propagation simulation technique is largely independent of the waveguide geometry and input wavelength.

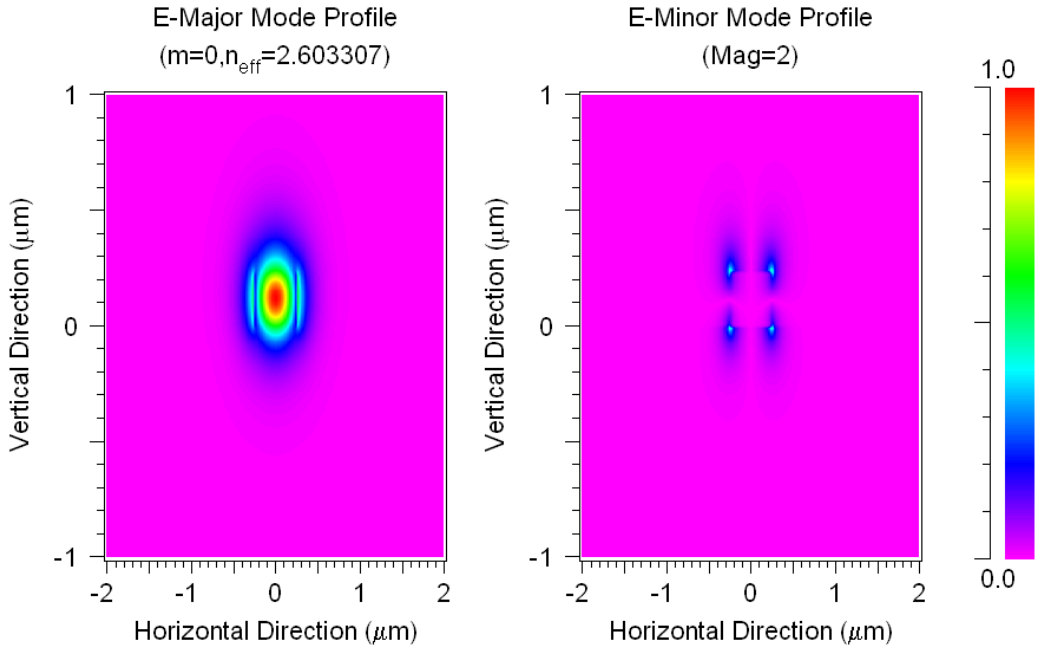

Figure 18: Beam propagation mode calculation
Rsoft 3D vector BEAMPROP simulation for a buried rectangular waveguide. Colour map shows the magnitude of corresponding electric field. Height of 300 nm, width of 500 nm.

Figure 18 is the output of one beam propagation simulation. For a given waveguide structure, cover index, height, width, and free space wavelength, a beam propagation simulation can be run and the propagation constant and EM field structures of the first bound mode found. For our studies, these simulations were run in parallel each with a slight variation. Six structures were simulated this way to study the predicted sensitivity of each type of guiding structure - a strip waveguide, two rib waveguides with varied slab height, and three buried waveguides with varied oxide cover thickness.

The beam propagation simulation results for four waveguide structures are shown in Figure 19. Visually, the buried waveguide structure experiences the smallest shift in propagation and the strip waveguide possess the largest as the cover index of refraction is increased. The simulated waveguide structures

have the same height and width (300 nm and 500 nm respectively). As with the 3-slab simulations, every waveguide structure is predicted to show an increase in peak location with increasing cover index of refraction. The critical factor of the magnitude of these shifts is the type of guiding structure used.

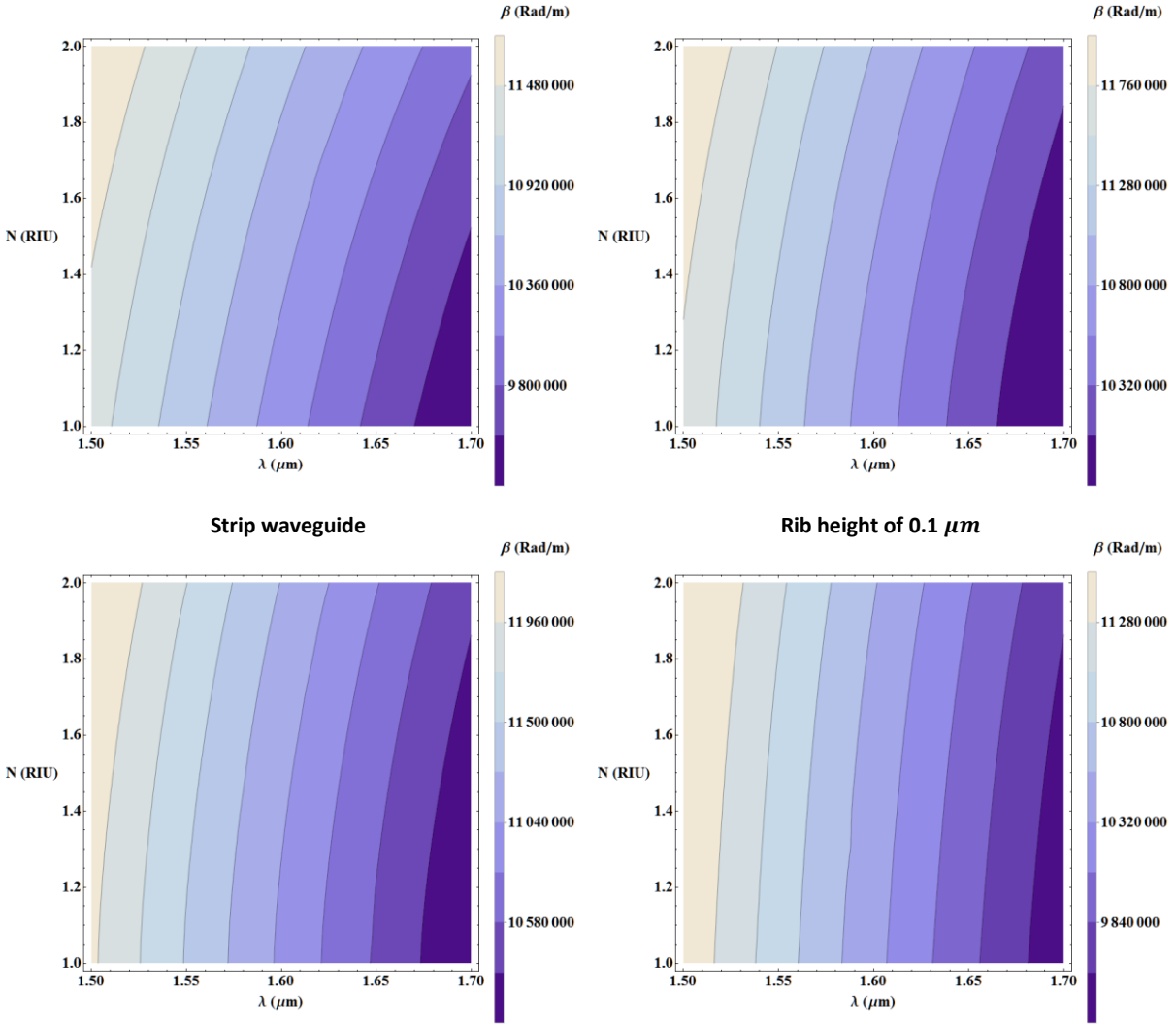

Figure 19: BEAMPROP propagation constant simulations

Propagation constant vs wavelength (μm) and cover index on the x and y axes, respectively. All propagation constants were calculated through a 3D vector beam propagation simulation. All of the simulated structures have the same height (0.3 μm) and width (0.5 μm).

4.2 Resonator Sensor Structure Analysis

Peaks

The resonator transmission equation, (64), possesses a minimum when $\beta L = 2m\pi$ corresponding to constructive interference for a round trip in the ring structure. In the idealized spectrum the dispersion relation is approximated by $\beta = 2\pi n_{eff}/\lambda$. Figure 20 shows the idealized transmission spectrum of a resonator with path length 120 µm and a constant effective mode index of 2.5. If we assume that the

device is thermally isolated then only changes in the propagation constant will result in changes in the transmission spectrum. The sensing arm of a resonator device is the ring path. As a constant multiplier to the effective index is increased, increasing the effective index, resonance peaks shift to the right. This is the direction of shift we expect from the sensor corresponding to an increase in propagation constant due to changing cover index of refraction.

$$\left|\frac{b_1}{a_1}\right|^2 = \frac{a^2 + t^2 - 2at\cos(\beta L)}{1 + a^2t^2 - 2at\cos(\beta L)} \quad (64)$$

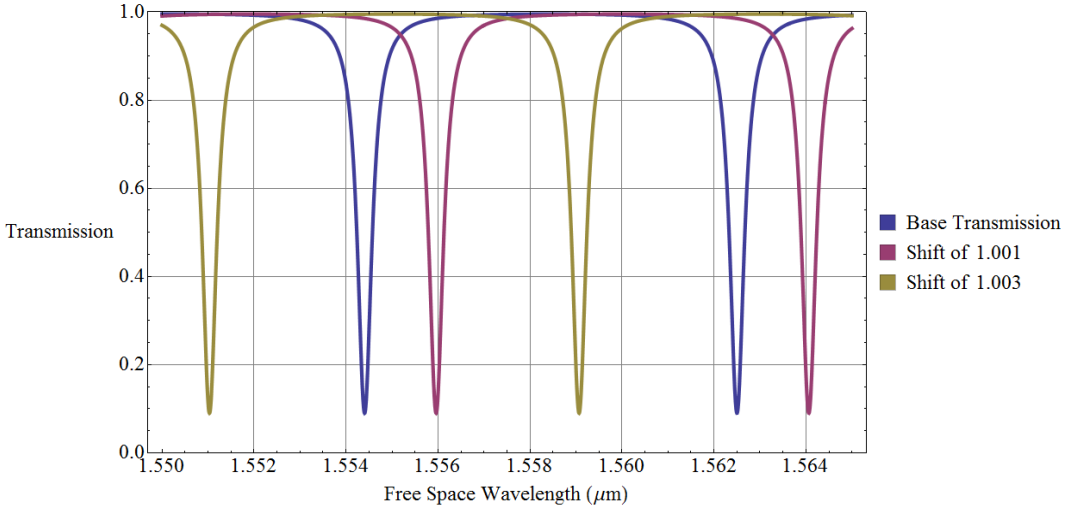

Figure 20: Idealized resonator transmission

L=120 um t=0.91 α=0.95 effective index 2.5, with a constant shift applied to the propagation constant

In order to use the peak location of a resonator as an indicator for changes in cover index of refraction, this effect must be further studied to find ways to control sensitivity. The beam propagation and three layer slab simulation data will be used to model the effects of changing cover index. From the simulation data we seek to quantify the expected shift in peak location resulting from changes in the cover index of refraction.

Peak Location

The movement of the resonance peaks is predicted by level sets of the dispersion relation with varying cover indices of refraction and free space wavelengths. As the cover index of refraction is increased both the beam propagation and three layer slab simulations predict an increase in β. The results of these simulations are shown in Figure 19. The sensitivity is strongly dependent on the waveguide geometry, with structures that have more evanescent field exposed to the air having larger sensitivities. All of the expected shifts in resonance peak are positive.

When used as a sensing device the resonator is not physically changing its shape. The length is constant and the new minimum will occur at a wavelength that produces a mode with the same propagation constant as when the cover index of refraction was unchanged. This ensures that the bound mode accumulates the same phase change over one path length of the resonator, equation (65). The expected sensitivity for a resonator sensor is the slope of the level sets of the dispersion relation and is given by equation (67). These partial derivatives can be numerically evaluated with the simulated data.

$$\boldsymbol{\beta(\lambda, N)L = 2m\pi} \quad (65)$$

$$\boldsymbol{D\beta = 0 = \frac{\partial \beta}{\partial N} dN + \frac{\partial \beta}{\partial \lambda} d\lambda} \quad (66)$$

$$\boldsymbol{\frac{d\lambda}{dN} = -\frac{\left(\frac{\partial \beta}{\partial N}\right)}{\left(\frac{\partial \beta}{\partial \lambda}\right)}} \quad (67)$$

For a resonator device with a fraction x of the resonator path exposed to changes in cover index, the phase gained over one round trip is given by equation (68). The subscript c represents the covered portion of the resonator path, not affected by changes in the measurand, and the subscript v represents the exposed portion. A first order expansion of the propagation constant functions yields the expected sensitivity, equation (70). The presence of x in the numerator is the major difference between this and equation (67). The particular resonator tested in this thesis has half of the resonator path exposed to the air. The interferometer studied in [19] examined the trade-off between layer thickness and sensor sensitivity, showing a 10% change in sensitivity with the presence of a $10\ nm$ SiO_2 layer.

$$\boldsymbol{\beta_c(\lambda)L(1-x) + \beta_v(\lambda, N)Lx = 2m\pi} \quad (68)$$

$$\boldsymbol{\frac{d\beta_c}{d\lambda} d\lambda\, L(1-x) + \left(\frac{\partial \beta_v}{\partial \lambda} d\lambda + \frac{\partial \beta_v}{\partial N} dN\right) Lx = 0} \quad (69)$$

$$\boldsymbol{\frac{d\lambda}{dN} = -x\left(\frac{\partial \beta_v}{\partial N}\right) \Big/ \left(\frac{d\beta_c}{d\lambda}(1-x) + \frac{\partial \beta_v}{\partial \lambda} x\right)} \quad (70)$$

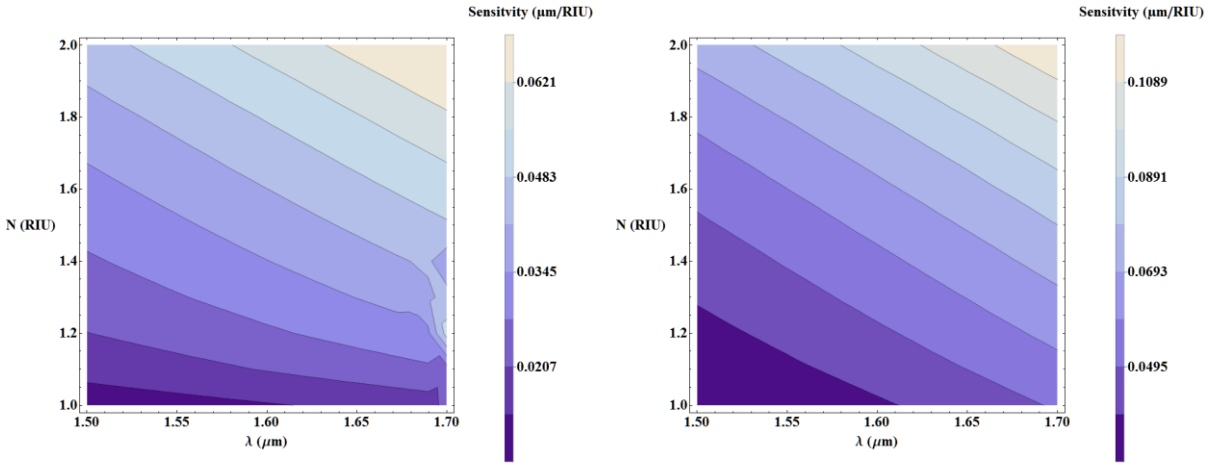

Height 0.3 μm, width 0.5 μm, rib height 0.1 μm **Height 0.22 μm, width .5 μm, slab height 0.05 μm**

Figure 21: Simulated waveguide sensitivity

Rib waveguide sensitivity to cover refractive index change. Units of graph are μm/RIU. Data came from 3D vector BEAMPROP simulations.

Figure 21 shows the expected sensitivity, from equation (67), for two of the waveguide structures simulated. From this figure the beam propagations simulations predict an increase in sensitivity as the cover index increases as well as an increase in sensitivity with increased wavelength.

The interpolating function can be used to track the location of a particular value of β, and hence a resonance peak, as the cover index is changed. Figure 22 shows the shift, measured from the original wavelength, of three propagation constants against the change in cover index of refraction for various waveguide geometries. All simulations predict a positive shift in peak location as the cover index of refraction is increased, and that the defining factor in the magnitude of the shift is the geometry of the exposed waveguide. The strip waveguide expected a sensitivity of $45\ nm/RIU$ while the $1\ \mu m$ buried waveguide predicts a sensitivity of only $2\ nm/RIU$. [20] studies the effect of waveguide geometry and coupling distance on a ring resonator sensor's sensitivity. The ring resonator structure tested in [21], a rib waveguide with a height of $220\ nm$, width of $450\ nm$ and rib height of $27\ nm$, reported a sensitivity of $70\ nm/RIU$. A sensor composed of two resonators in series reported a sensitivity of $1300\ nm/RIU$ in [22].

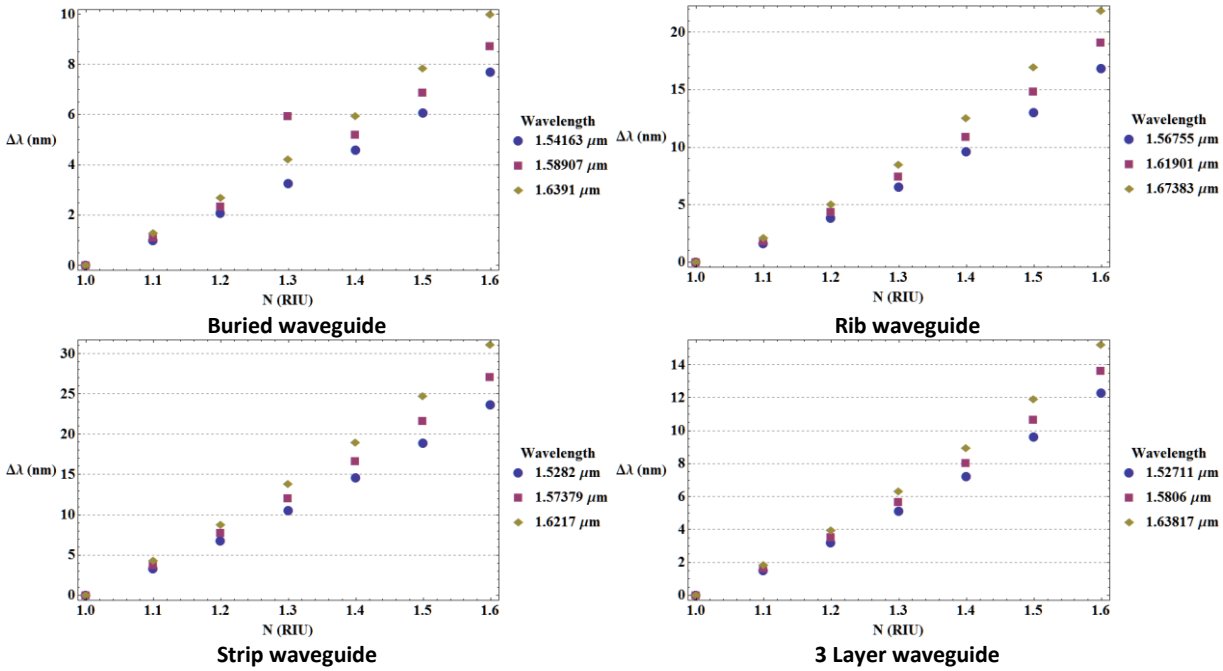

Figure 22: Shift in peak location vs cover index of refraction

Covered, rib, and strip waveguide and three layer slab simulated dispersion relations. Three values of β were arbitrarily chosen, and their respective wavelength with cover index 1.0 are given in the legend. Data came from 3D vector BEAMPROP simulations.

Free Spectral Range

Along with the peak location, the FSR can also be measured with the same sweep measurements. In terms of the dispersion relation the FSR can be found by choosing two values of β that satisfy $\beta_1 L = 2\pi m$ and $\beta_2 = 2\pi(m+1)$. Just as we tracked the movement of one resonance peak with interpolating functions, the FSR (as a function of cover index) can be extracted from the beam propagation simulations. The predicted change in FSR from BEAMPROP simulations for various waveguide structures are shown in Figure 23.

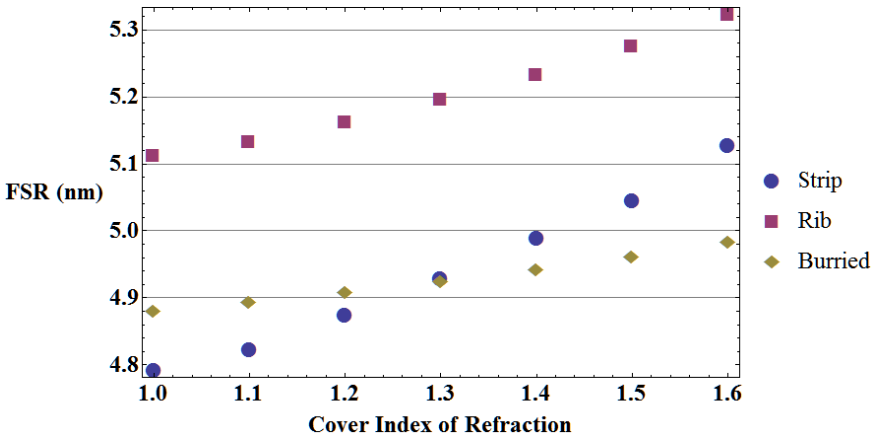

Figure 23: FSR vs cover index from BEAMPROP simulations

The nearest peak to 1550 nm was chosen for each dataset. Data came from 3D vector BEAMPROP simulations.

All simulations, with the exception of the covered waveguide, predict an increase in FSR of a magnitude that is detectible by a swept laser. This change can be used to decrease the sweep range required to make measurements, removing ambiguity caused by the periodic nature of the transmission of the resonator structure.

4.3 Predictions

The beam propagation simulations for varied waveguide structures suggest that the strip wave guide is more sensitive to variations in cover index of refraction than the buried or rib waveguides. It had a predicted sensitivity of 45nm/RIU and also has the largest variation of FSR with changes to cover index. The predicted shift of the resonance peak is independent of the length of the resonator.

Figure 24 shows the expected shift of resonance peak for a waveguide with the dimensions of those tested in this thesis as a function of cover index or refraction. It was a rib waveguide with height 220 nm, width 500 nm, and slab height of 50 nm. The expected sensitivity is 48.8 nm/RIU at a wavelength of 1557 nm. However, since only half of the resonator structure is exposed to the air, the predicted sensitivity of this sensor is 24.4 nm/RIU. Compared to a taller rib waveguide, the shorter structure is expected to have a higher sensitivity.

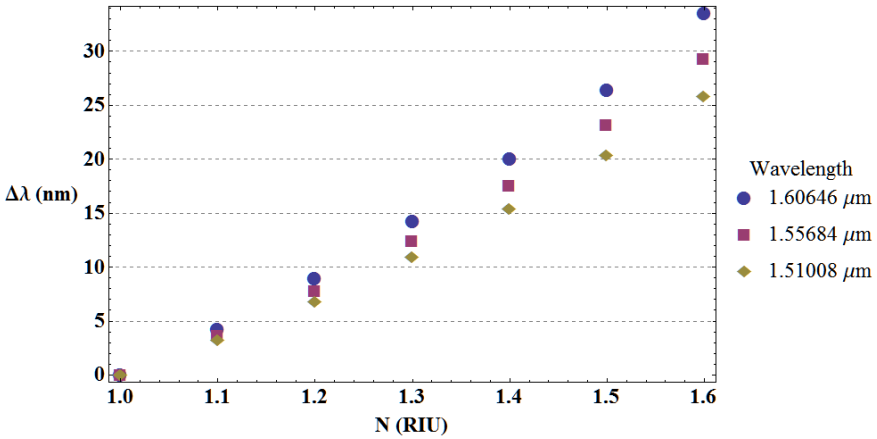

Figure 24: Expected shift of waveguide structure

From BEAMPROP simulation of waveguide dimensions used in sensor. Data comes from 3D vector BEAMPROP simulation.

5 Results

5.1 Experimental Setup

Data was collected with an automated labview program which controlled a tuneable laser while making simultaneous measurements of optical output power. The resonator structures, along with connecting waveguides and grating couplers, were etched on a silicon wafer. Bare fibre cores, held securely to micro manipulators, are positioned above the silicon chip and held at 10° so that laser light can be coupled between the fibre core and the grating coupler. Given a specified optical range and wavelength step size the labview program generates the transmission spectrum of the connected structure.

The angle and quality of cut of the bare fibre are critically important to the quality of the power transmission at the two couplers on the device. The inspection of the fibre cuts as well as their initial positioning was done visually with the aid of a microscope. Once the laser is turned on, if the initial positioning of the fibres is close enough to the grating couplers, the optical power meter will read power exiting the chip. Small adjustments are made to both the input and output fibre coupling positions to maximize the transmitted power.

Once the baseline measurements of the device are made for a cover index of refraction of 1, different liquids can be placed on the chip and the change in peak location can be observed. If the chip moves as the sample liquid is placed on its surface, preventing light coupling through the grating, then the chip must be cleaned and the process restarted. The diffraction caused by the presence of the liquid makes it impractical to visually align the bare fibres on top of the grating coupler.

The chip was cleaned by pipetting alcohol onto the chip multiple times, in multiple directions, wiping away excess with a delicate tissue and blow drying it. The chip can then be reconnected to the experimental equipment to see how close the measured resonator peaks are to the baseline values. Some of the index matching fluids were removed easily, while others did not entirely come off the chip at all. A second chip was used to complete the last half of the sensing trails because the index matching fluid in the second trial did not clean off well.

5.2 Device Geometry

The structure to be tested as a sensor is a ring resonator. Ten nearly identical structures were manufactured on the silicon chips used. Of these, the fourth one down had the most consistently good power coupling, and so was the used in the trials.

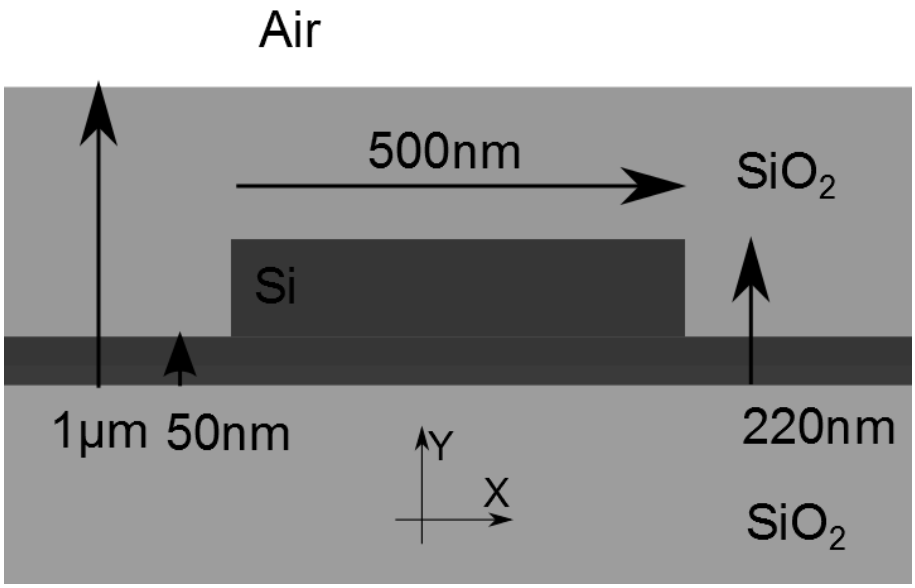

Figure 25: Cross section of waveguide
Geometry of waveguide in SOI chip tested as sensor.

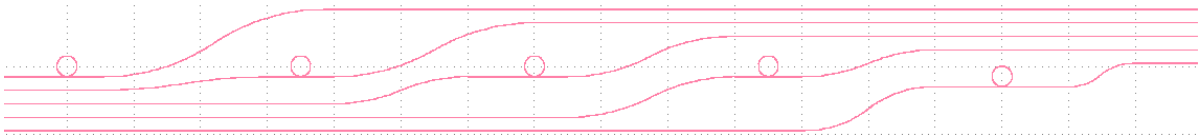

Figure 26: Screen capture of chip's CAD file
Array of manufactured rings on one SOI chip. Grating couplers omitted.

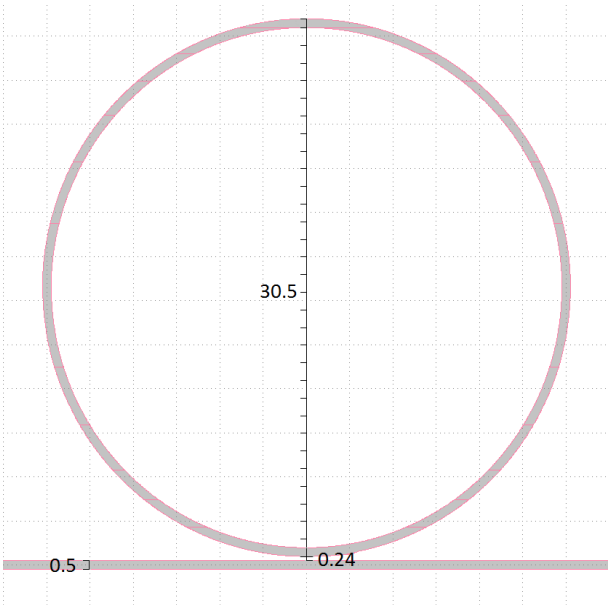

Figure 27: Close-up of ring structure
30.5 μm in diameter, coupling distance of 0.24 μm with strip waveguide. Half exposed to air.

Both chips used in this study had rib waveguides fabricated on top of a 2 μm oxide layer. The total height of the rib waveguide is 220 nm, with a rib height of 50 nm and width of 500 nm shown in Figure 25. A 70 nm secondary etch formed the grating couplers. The chips were produced in France by CEA-LETI using a 193 nm deep UV lithography. The index of refraction of silicon is near 3.44 and the refractive index of silicon dioxide is near 1.43. The ring resonator structures used in the study are shown in Figure 26 and Figure 27. The diameter of the rings was 30.5 μm and the smallest coupling distance was 240 nm.

5.3 Resonator Peaks

With the output power plotted on a log scale, the location of the resonator peaks is clearly visible. The positive shift predicted by the simulations was observed. The wavelength sweep of the experiment was from 1550 nm to 1565 nm in steps of 0.05 nm. Three power outputs were averaged per input wavelength to create one data point on the wavelength sweep. The dwell time for each measurement was 50 ms. Figure 28 shows the baseline response of the resonator structure.

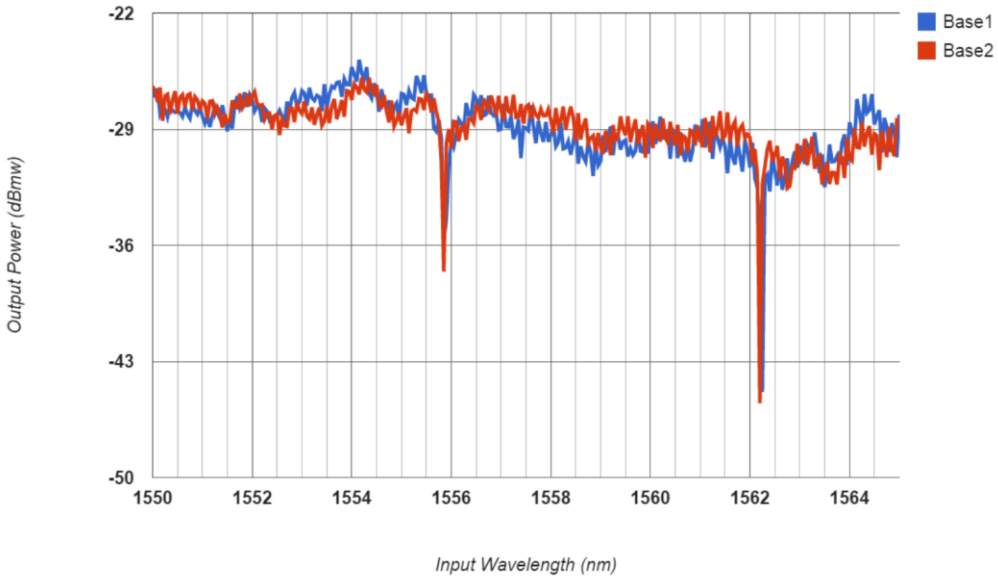

Figure 28: Initial frequency response of resonator for chip #1

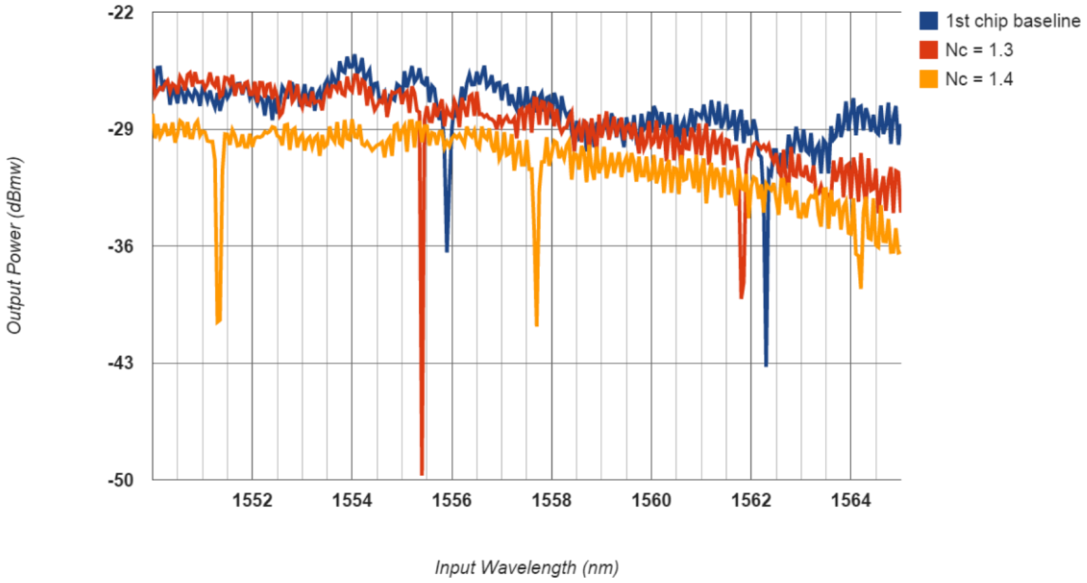

Figure 29: Swept response with various liquids for chip #1

Figure 29 shows the baseline spectrum response and the shifted response due to the presence of two index matching fluids on the surface of the chip. The uncertainty in the stated refractive index of the index matching fluids was 0.0002 RIU. The 1.4 index matching fluid was not easily cleaned off so a second resonator structure, of the same geometry, was employed for further tests. Its base spectrum is shown below in Figure 30. The chip was etched on a piece of silicon from a different position of the wafer, and its impurity level is slightly different than the first chip tested. This may account for the slightly different resonance peak locations. Figure 31 shows the shifted response due to the presence of the remaining two liquids tested, with N=1.5 RIU and N=1.6 RIU.

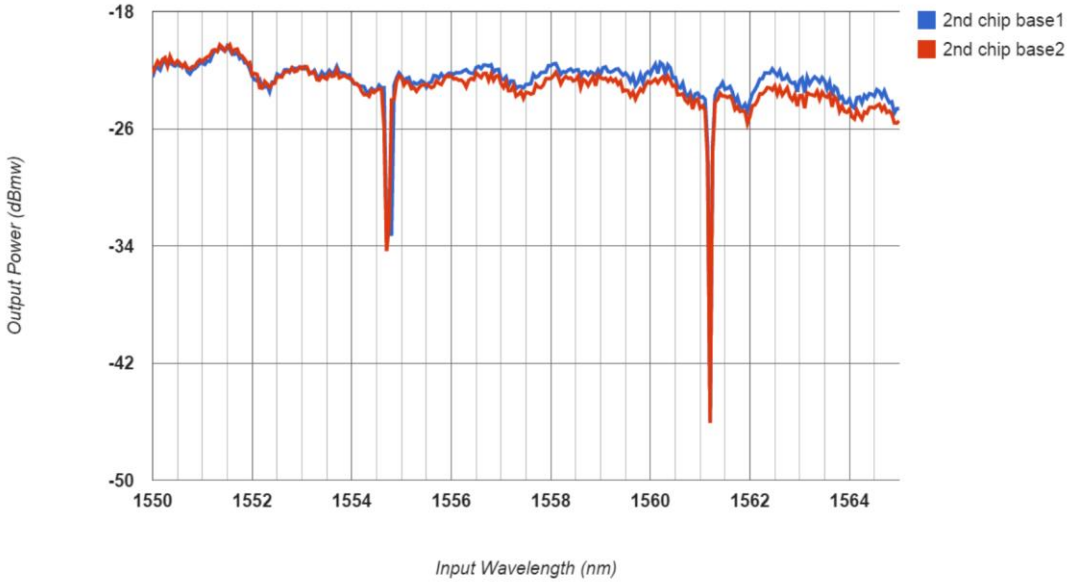

Figure 30: Initial frequency response of resonator for chip #2

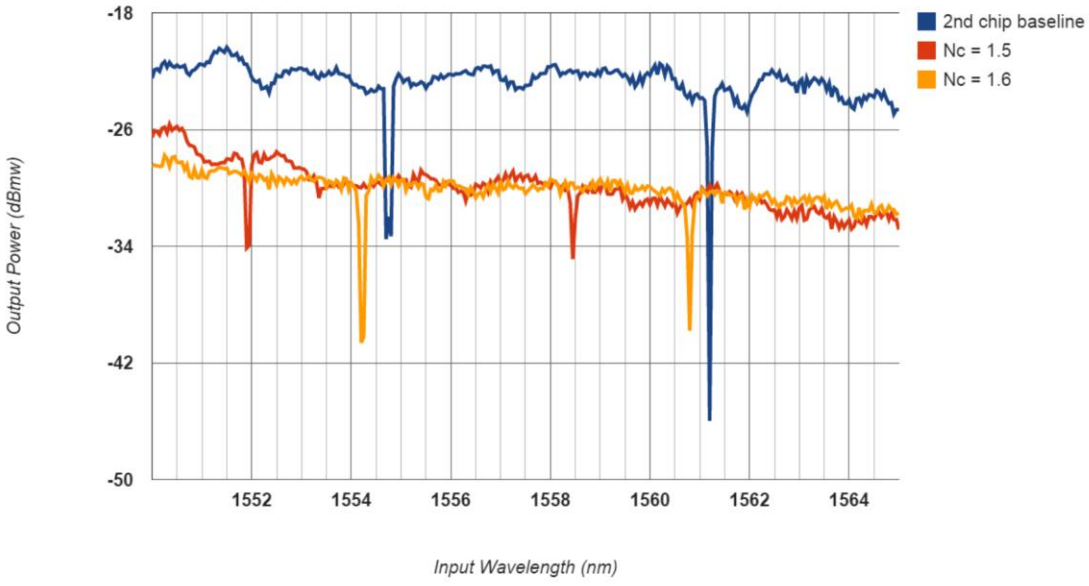

Figure 31: Swept response with various liquids for chip #2

The shift of the resonance peaks exceeds both the FSR of the ring and the sweep range of the test for tests on the second chip. The scan spectrum was chosen to be slightly larger than twice the ring's FSR

so that at least two peaks are always visible. The location of the peaks was determined by choosing the wavelength reading with the lowest transmitted power, or by averaging between adjacent values if the output power is of the same magnitude. Shifts beyond the scan range were tracked by finding the location of the nearest peak and adding the measured baseline FSR.

When drying the chip between applications of the index matching fluid the most accurate procedure for establishing if the chip's sensing area is clean was to compare the peak location to a baseline value. The more times the chip was washed and dried the closer to baseline value the measured peak became. These plots allow us to see the unshifting of the sensor as the residue layer deposited by the index matching fluid is slowly removed.

Figure 32 details the recovery of the resonator sensor as a function of the number of times the chip was dried. As the time spent drying increases the peak location gradually shifts back toward the baseline value. The peak location for the 7th and 8th drying steps did not change between cleanings, but was observed to shift closer to the base value after approximately 12 hours of waiting. The shift observed between the 8th and 9th drying measurement is due to the residual heat from the cleaning step.

Even after five cleanings the shift in resonance peak was significant - even the final test was not exactly in line with the baseline value. This shows that this device is very sensitive to residue, most likely due to the shape in which the oxide layer was etched away from the ring.

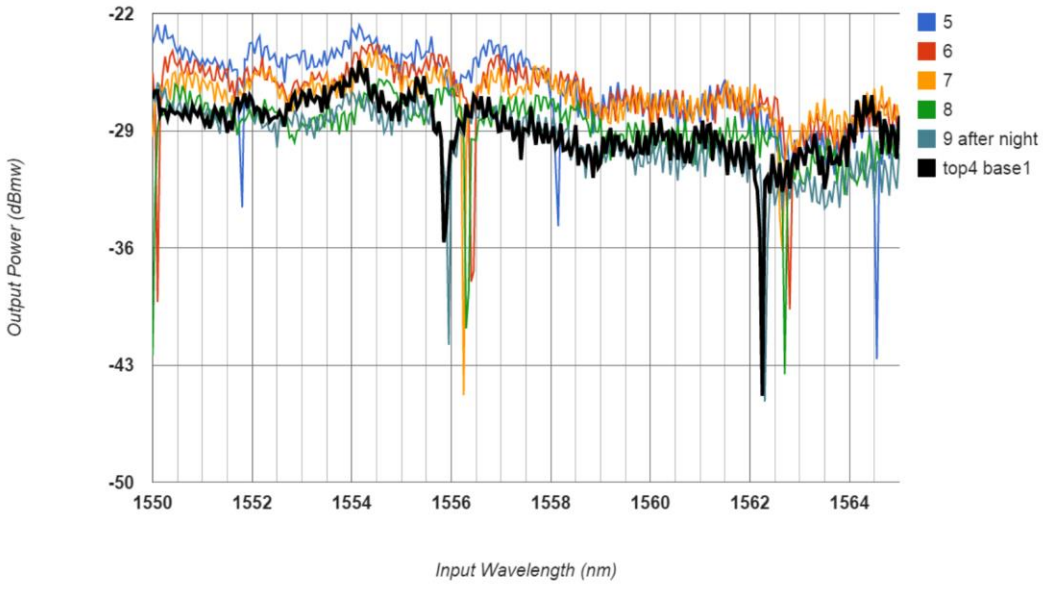

Figure 32: Resonator spectrum during cleaning
Series differentiates the number of times the chip was cleaned then dried with a blow-dryer

5.4 Shift vs Cover Index

Tracking the peak at 1555.9 nm, we observe an increase in the peak location to 1561.8 nm and 1564.2 nm when liquids with indices of refraction with values of 1.3 RIU and 1.4 RIU respectively are applied. The peak at 1554.75 nm on the second chip increases to 1565 nm and 1567.4 nm when cover indices of 1.5 RIU and 1.6 RIU respectively are applied. When these shifts are plotted they show a clear linear relationship. The uncertainty of the measurement can be calculated from the laser step size and the slope uncertainty.

Cover index	Start (nm)	Shifts to (nm)	Shift of (nm)
1	1555.9±0.025	1555.9±0.025	0±0.04
1.3	1555.9±0.025	1561.82±0.025	5.92±0.04
1.4	1555.9±0.025	1564.18±0.025	8.28±0.04

Peak analysis of first chip

Cover index	Start (nm)	Shifts to (nm)	Shift of (nm)
1	1554.75±0.025	1554.75±0.025	0±0.04
1.5	1554.75±0.025	1558.45±0.025+6.55±0.04	10.25±.05
1.6	1554.75±0.025	1560.8±0.025+6.55±0.04	12.60±.05

Peak analysis of second chip

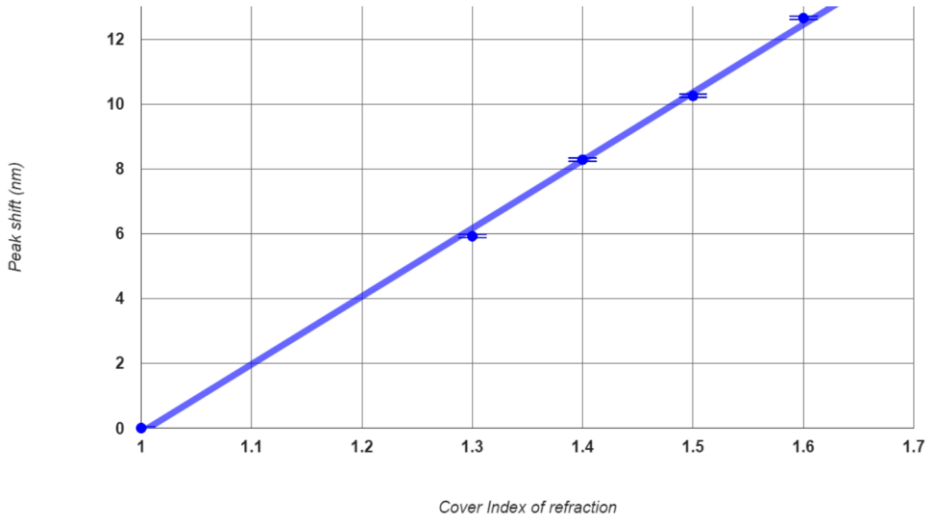

Figure 33: Resonator peak shift vs cover index of refraction

The experimental relation between the peak shift and cover index is shown in Figure 33. In particular, the slope (sensitivity) of the structure for the wavelength region 1550 nm to 1565 nm was measured to be 21 nm/RIU with an uncertainty of 0.44 nm/RIU (2.1%) and the r^2 value of the linear fit was 0.998. This is in good agreement with the expected sensitivity of 24.4 nm/RIU.

5.5 Free Spectral Range Change

Beyond observing the shift in resonance peak relative to baseline values, adding an index matching fluid produced an observable increase in the FSR of the device in good agreement with the simulation predictions.

Cover Index	Peak 1 (nm)	Peak 2 (nm)	FSR (nm)
1	1562.3±0.025	1555.9±0.025	6.4±0.04
1.3 (next peak to the left)	1561.82±0.025	1555.4±0.025	6.42±0.04
1.4	1564.18±0.025	1557.7±0.025	6.48±0.04
1	1561.2±0.025	1554.75±0.025	6.45±0.04
1.5 (two peaks to the left)	1558.45±0.025	1551.925±0.025	6.55±0.04
1.6	1560.8±0.025	1554.2±0.025	6.6±0.04

Table of FSR shift

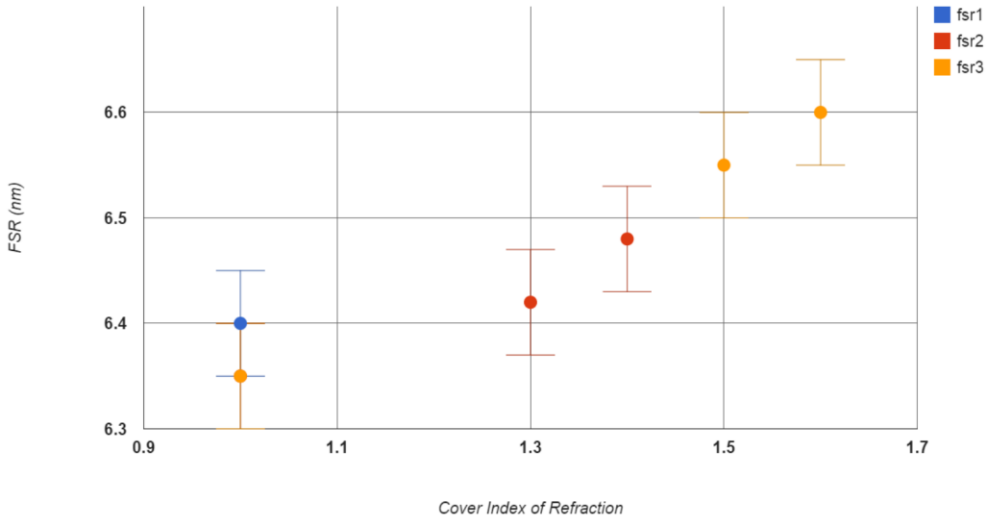

Figure 34: FSR change as a function of cover index of refraction
Different series distinguish the change in FSR for each pair of peaks within the swept area. Blue series is original pair of peaks in swept range, Red is second pair of peaks and yellow is the third.

Figure 34 displays the FSR of the peaks observed in the sensor sweep for each application of the index matching fluid. The blue series shows the baseline measurement of chip 1. The application of the 1.3 RIU index fluid displaces the rightmost peak beyond the sweep range and the red series distinguishes this pair of peaks from the baseline value. Similarly, the application of the 1.5 RIU index matching fluid displaces the baseline by an amount such that the FSR measurement made is that of the second pair of peaks to the left of the baseline of the second chip, and is shown by the yellow data series. The unshifted FSR was obtained from the data in Figure 35. The BEAMPROP simulations predicted an increase of about 0.2 nm with the application of a 1.6 RIU index matching fluid. This is in close agreement with the observed shift of 0.25 nm.

The benefit gained by the sensor from measuring the FSR, in addition to the shift in resonance peak, is that this change, which is also dependent on the cover refractive index, can be used as an indicator to remove the ambiguity of a shifted spectrum beyond the FSR of the ring. The two high value index matching fluids used to calibrate the sensor produced readings that could be misinterpreted as liquids of refractive index lower than 1.3 RIU. The change in FSR in these measurements removes this ambiguity.

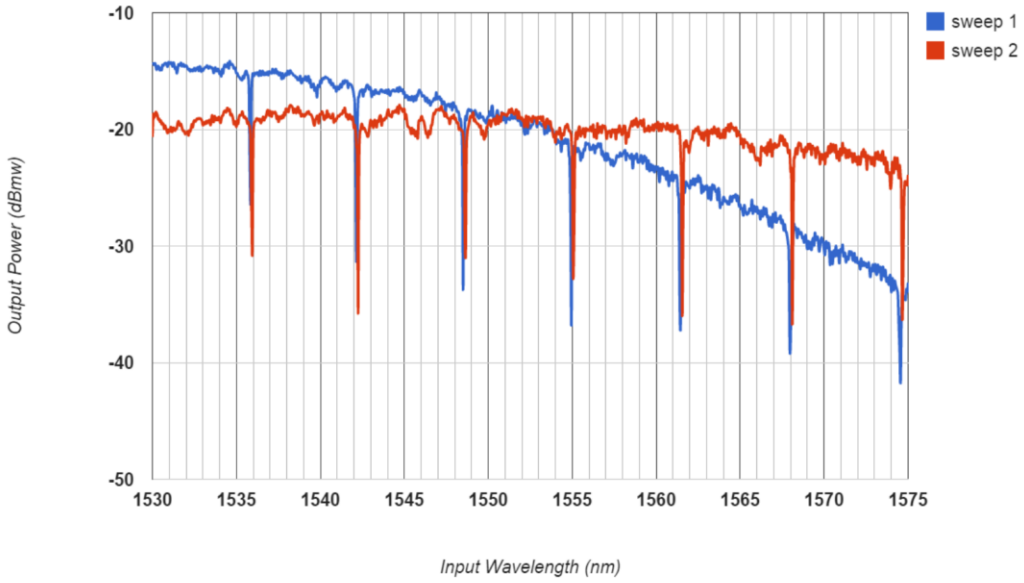

Figure 35: Spectral response of resonator on chip #2
Broad spectrum sweep with step size $0.05nm$

5.6 Temperature Effect Due to Evaporation

Earlier in the data collection another resonator structure was tested. This chip had identical components (grating couplings and a ring resonator with path length $205\ \mu m$) but had a much thicker oxide protective cover layer. When the experiments outlined above were performed on this chip with alcohol as the liquid, a shift in resonance peak was observed despite the cover being too thick for changes in the surface index of refraction to influence the propagation constant of the bound modes of the waveguide. These findings are summarized in Figure 36. This effect was found to be caused by the temperature change due to the evaporation of the alcohol. This was discovered when tests with the index matching fluids (which do not evaporate at room temperature) caused no change in the location of the resonance peaks.

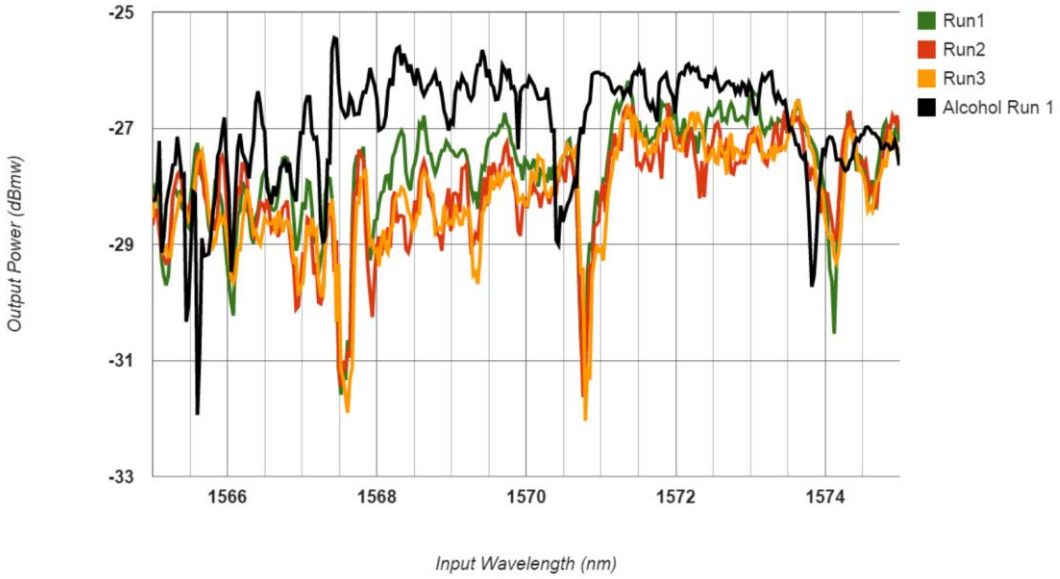

Figure 36: Shift observed due to temperature change
Temperature change caused by alcohol evaporating from the surface.

Since evaporation is an endothermic reaction the surface of the chip, and therefore the ring structure, cools off and will contract as a result. Since the geometry induced phase change is βL the resonance peaks will occur at wavelengths that produce larger β, corresponding to a negative shift in wavelength.

The change in path length can be deduced from the shift in wavelength. Assuming the propagation constant is given by $2\pi n_{eff}/\lambda$, any change in length of the resonator can be approximated by equation (71). If L_2 is less than L_1, as with the case for a shrinking resonator, we would expect the new resonance peak to occur at a lower wavelength. This approximation of the change in path length can be employed in conjunction with the spectral measurements to eliminate any temperature effects from the environment or the evaporating sample as it provides a new baseline value.

$$\boldsymbol{L_2 = L_1 \frac{\lambda_2}{\lambda_1}} \qquad \textbf{(71)}$$

Using the change in resonance peak and the thermal expansion coefficient of silicon, $2.6 * 10^{-6}\ K^{-1}$ [23], the change in surface temperature is approximately 81 degrees.

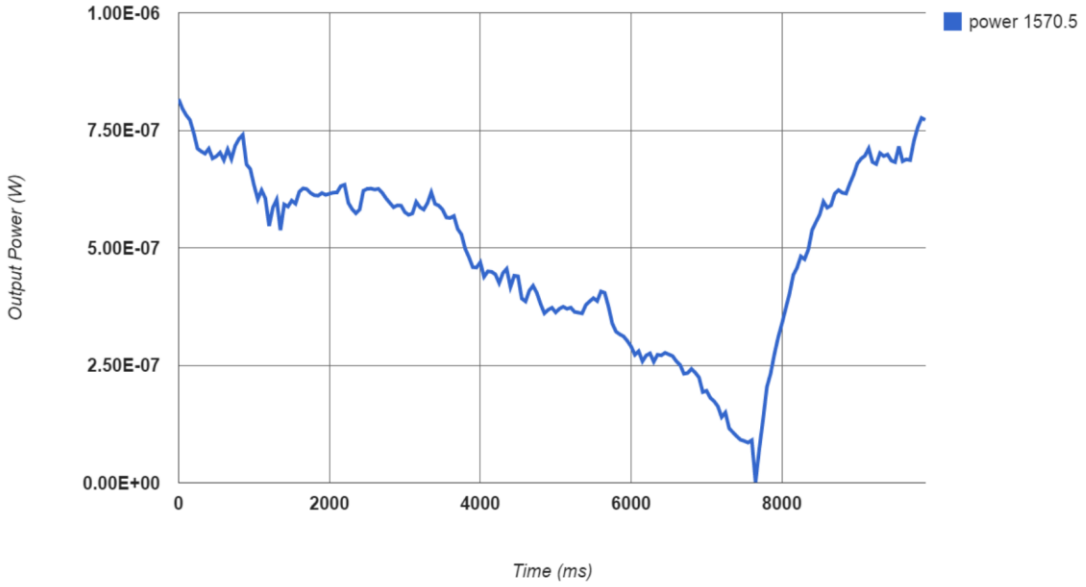

Figure 37: Power vs time for wavelength adjacent to resonance peaks
Temperature change caused by alcohol evaporating from the surface.

This shift was further examined by tracking the output power of the structure as a function of time for a wavelength in-between the baseline and shifted peak locations caused during cooling by the evaporating alcohol (Figure 37). Since this chip was not designed with a reference arm it is difficult to interpret these measurements as a practical measurement method for evaporation rate, but the peak position clearly shifts downward as time progresses and back up after the evaporation ceased at 8000 ms.

Such measurements, when compared to a reference power, can be used to measure small changes in the resonance peak location. The measurement of transmitted power of a wavelength in the path of the shift in resonance wavelength indicates the magnitude of this shift with a very high accuracy. For a sensor with a reference arm the measured value used to determine the measurand is the ratio of power in the reference and sensing arms. A narrower peak (greater finesse) will cause a larger change in the observed power ratio when compared to a broader peak for the same shift in peak location.

5.7 Uncertainty

The linear dependence of the resonance wavelength on cover index (equation (72)) can be employed to determine the cover index of refraction according to equation (73). N is the cover index of refraction, M is the slope of the linear fit used to calibrate the sensor and $\Delta\lambda$ is the predicted shift in resonance peak.

$$\Delta\boldsymbol{\lambda} = (\boldsymbol{N} - \mathbf{1})\boldsymbol{M} \quad (72)$$

$$\boldsymbol{N} = {}^{\boldsymbol{\Delta\lambda}}/_{\boldsymbol{M}} + \mathbf{1} \quad (73)$$

The uncertainty of the device, the precision with which the measurand can be determined, for a sweep step of 0.05 nm, is dominated by the uncertainty in the slope. The percentage uncertainty in wavelength measurements is, in the wavelength range tested, 0.025 nm/1550nm or .0016%. From the data collected, this ring resonator has a sensitivity of 2.1% for a measurement of a liquid of index 1.3 RIU the uncertainty is 2.1% of 1.3 or 0.027 RIU.

6 Conclusion

In this thesis the shift in spectral response of a SOI ring resonator due to changes in cover index of refraction was characterized in order to establish the viability of the structure as a sensor. This was demonstrated both through computer simulations and experimental measurements. A simple sensor composed of a ring resonator, half exposed to the air, was tested and the measured sensitivity was in close agreement with the computer simulations. The observed sensitivity of the half covered ring structure was 21 nm/RIU, close to the predicted value of 24.4 nm/RIU from BEAMPROP simulations.

It was also demonstrated that the change in FSR, resultant from the increase in cover index of refraction, was detectable on the SOI chip tested. This change in FRS is a second indicator for changes in the measurand of the sensor. When used in conjunction with the shift in peak location, the change in FSR can be used to extend the measurement range of the sensor beyond the FSR, eliminating a sacrifice in sensitivity to increase operational range. Computer simulations of the basic waveguide structures suggest that strip waveguides have the highest sensitivity to both peak location and FSR due to changes in cover index of refraction.

From the analysis of the variation in resonance wavelength due to temperature changes caused by evaporation, a ring resonator device could be designed to measure cover thickness during evaporation by making use of both covered and uncovered sensors. The covered portion would indicate changes in temperature and therefore path length, and the uncovered sensor will measure changes in propagation constant and therefore layer thickness. Since the covered sensor's output is only affected by changes in temperature, any influence of the temperature on the measurement can be isolated, assuming that the change in temperature is the same for both portions of the sensor. Finally we found, from drying the resonator multiple times, that impurities deposited from the drying of a sample on the sensing area are detectable.

Though the sensor structure studied in this thesis is not novel and the sensitivity not large, the computer simulations yielded accurate predictions for the sensor's performance. Tracking the change in FSR of the ring and using this to extend the active range of the sensor is a new development in the field. The model of a double ring sensor capable of making measurements during temperature changes is also an exciting development.

7 Future Work

Further work to develop sensing devices could include examining alternative waveguides and wavelength regimes. Papers studying whispering gallery resonators, band gap waveguides, photonic crystals and more narrow waveguide geometries all reported improved performance over that observed in this thesis.

Since neither of the chips tested possessed a reference arm, no power dependent sensor could be tested. Small changes in transmission spectrum could be detected if a reference power signal is available, resulting in high sensitivity measurements.

More complicated waveguide structures composed of resonators and interferometer in series could improve sensitivity, though at the expense of requiring a larger spectral range. Silicon nanoparticles suspended in a medium can be used as resonator structures as well [24]. Suspending nanoparticles in a liquid over the sensing area of the ring would be akin to coupling a second resonator [25]. Triangular resonators that can excite surface plasmons have also been designed to be sensors. Sensors typically are designed to have a cascade of sensing structures, allowing for averages of output values to decrease the uncertainty.

References

[1] F. L. Pedrotti and L. S. Pedrotti, Introduction to Optics, Second Editon, Englewood Cliffs, NJ: Prentice-Hall, Inc. , 1993.

[2] K. Kenji and T. Kitoh, Introduction to Optical Waveguide Analysis, John Wiley & Sons, 2001.

[3] D. Yevick, "A Guide to Electric Field Propagation Techniques for Guided-wave Optics," *Optical and Quantum Electronics,* vol. 26, no. 3, 1994.

[4] Buckman, Guided-Wave Photonics, Saunders College, 1992.

[5] O. Frazao, J. M. Baptista and J. L. Santos, "Temperature-Independent Strain Sensor Based on a Hi-Bi Photonic Crystal Fiber Loop Mirror," *IEEE Sensors Journal,* vol. 7, no. 10, pp. 1453-1455, 2007.

[6] Gong, Huaping, C. C. Chan, L. Chen and X. Dong, "Strain Sensor Realized by Using Low-Birefringence Photonic-Crystal-Fiber-Based Sagnac Loop," *IEEE Photonics Technology Letters,* vol. 22, no. 16, pp. 1238-1240, 2010.

[7] T.-A. Massood, Optical Sensors, Kluwer Academic Publications, 1995.

[8] M. L. Notte and V. M. Passaro, "Ultra High Sensitivity Chemical Photonic Sensing by Mach–Zehnder Interferometer Enhanced Vernier-effect," *Sensors and Actuators B: Chemical,* vol. 176, pp. 994-1007, 2013.

[9] Z. Wang, J. Yao, G. Yuan and L. Yang, "Analysis of Optical Sensing Behavior of a Novel Optical Bean-shaped Resonator Biosensor Integrated with MZI Configuration," *Journal of Modern Optics,* vol. 61, no. 13, pp. 1103-1108, 2014.

[10] G.-Y. Oh, D.-G. Kim, S. H. Kim, H. C. Ki, T. U. Kim and Y.-W. Choi, "Integrated Refractometric Sensor Utilizing a Triangular Ring Resonator Combined With SPR," *IEEE Photonics Technology Letters,* vol. 26, no. 21, pp. 2189-2192, 2014.

[11] T. Claes, J. Molera, K. De Vos, E. Schacht, R. Baets and P. Bienstman, "Label-Free Biosensing With a Slot-Waveguide-Based Ring Resonator in Silicon on Insulator," *IEEE Photonics Journal,* vol. 1, no. 3, pp. 197-204, 2009.

[12] C. Ciminelli, D. Dell'Olio, D. Conteduca, C. Campanella and M. Armenise, "High Performance SOI Microring Resonator for Biochemical Sensing," *Optics & Laser Technology,* vol. 59, pp. 60-67, 2014.

[13] Hsiao, Fu-Li and Chengkou Lee, "Novel Biosensor Based on Photonic Crystal Nano-Ring Resonator," *Procedia Chemistry,* vol. 1, no. 1, pp. 417-420, 2009.

[14] C. Li, S.-J. Qiu, Y. Chen, F. Xu and Y.-Q. Lu, "Ultra-Sensitive Refractive Index Sensor With Slightly Tapered Photonic Crystal Fiber," *IEEE Photonics Technology Letters,* vol. 24, no. 19, pp. 1771-1774, 2012.

[15] P. Sudeshna, G. Guillermain, R. Sriram, B. L. Miller and P. M. Fauchet, "Silicon Photonic Crystal Nanocavity-coupled Waveguides for Error-corrected Optical Biosensing," *Biosensors and Bioelectronics,* vol. 26, no. 10, pp. 4024-4031, 2011.

[16] Huang, Chu-Yu, W.-C. Wang, W.-J. Wu and W. R. Ledoux, "Composite Optical Bend Loss Sensor for Pressure and Shear Measurement," *IEEE Sensors Journal,* vol. 7, no. 11, pp. 1554-1565, 2007.

[17] Vijayan, Anu, Madhavi, V. Fuke, R. Karekar and R. Aiyer, "Planar Optical Waveguide Evanescent Wave CO2 Sensor Based on a Clad of Alstonia Scholaris Leaf Extract," *IEEE Sensors Journal,* vol. 9, no. 1, pp. 13-19, 2009.

[18] Shen, Yiran, I. B. Divliansky, D. N. Basov and S. Mookherjea, "Electric-field-driven Nano-oxidation Trimming of Silicon Microrings and Interferometers," *Optics Letters,* vol. 36, no. 14, p. 2668, 2011.

[19] A. Densmore, D. Xu, P. Waldron, P. Janz, J. Cheben, A. Lapointe, B. Delge, B. Lamontagne, J. H. Schmid and E. Post, "A Silicon-on-Insulator Photonic Wire Based Evanescent Field Sensor," *IEEE Photonics Technology Letters,* vol. 18, no. 23, pp. 2520-2522, 2006.

[20] Gou, Wei, F. Xu and Y.-Q. Lu, "Coupling Influence on the Refractive Index Sensitivity of Photonic Wire Ring Resonator," *Optics Communications,* vol. 285, no. 24, pp. 5144-5147, 2012.

[21] C. L. Arce, K. De Vos, T. Claes, K. Komorowska, D. Van Thourhout and P. Bienstman, "Silicon-on-Insulator Microring Resonator Sensor Integrated on an Optical Fiber Facet," *IEEE Photonics Technology Letters,* vol. 23.13, pp. 890-92, 2011.

[22] J. Lei, M. Li and J.-J. He, "Highly-sensitive Silicon-on-insulator Sensor Based on Two Cascaded Micro-ring Resonators with Vernier Effect," *Optics Communications,* vol. 284, no. 1, pp. 156-159, 2011.

[23] G. Eranna, Crystal Growth and Evaluation of Silicon for VLSI and ULSI, CRC Press, 2014.

[24] A. Serpengüzel and A. Demir, "Silicon Microspheres for Near-IR Communication Applications," *Semiconductor Science and Technology,* vol. 23, no. 6, 2008.

[25] A. T. Rosenberger, E. B. Dale, D. Ganta and J. P. Rezac, "Investigating properties of surfaces and thin films using microsphere," *SPIE Proceedings,* vol. 6872, 2008.

[26] J. M. Corres, R. M. Ignacio, H. Miguel, B. Javier and A. J. Francisco, "Optical Fiber Humidity Sensors Using Nanostructured Coatings of SiO2 Nanoparticles," *IEEE Sensors Journal,* vol. 8, no. 3, pp. 281-285, 2008.

[27] Huang and Wei-Ping, "Coupled-mode Theory for Optical Waveguides: An Overview," *Journal of the Optical Society of America,* vol. 11, no. 3, 1994.

[28] K. Isa, C. Kocabas and A. Aydinli, “Integrated Micro Ring Resonator Displacement Sensor for Scanning Probe Microscopies,” *Journal of Micromechanics and Microengineering,* vol. 14, no. 3, pp. 374-381, 2004.

[29] Liu, Jin, X. Zhou, Z. Qiao, J. Zhang, C. Zhang, T. Xiang, L. Shui, Y. Shi and L. Liu, “Integrated Optical Chemical Sensor Based on an SOI Ring Resonator Using Phase-Interrogation,” *IEEE Photonics Journal,* vol. 6, no. 5, pp. 1-7, 2014.

[30] D. G. Rabus, Integrated Ring Resonators: The Compendium, Springer, 2007.

[31] D. Rosenblatt, A. Sharon and A. Friesem, “Resonant Grating Waveguide Structures,” *IEEE Journal of Quantum Electronics,* vol. 33, no. 11, pp. 2038-059, 1997.

[32] K. DeVos, I. Bartolozzi, E. Schacht, P. Bienstman and R. Baets, “Silicon-on-Insulator Microring Resonator for Sensitive and Label-free Biosensing,” *Optics Express,* vol. 15, no. 12, p. 7610, 2007.

[33] I. M. White, H. Zhu, J. D. Suter, N. M. Hanumegowda, H. Oveys, M. Zourob and X. Fan, “Refractometric Sensors for Lab-on-a-Chip Based on Optical Ring Resonators,” *IEEE Sensors Journal,* vol. 7, no. 1, pp. 28-35, 2007.

[34] A. Yariv and M. Nakamura, “Periodic Structures for Integrated Optics,” *IEEE Journal of Quantum Electronics,* vol. 13, no. 4, pp. 233-253, 1977.

[35] A. Yariv, “Critical Coupling and Its Control in Optical Waveguide-ring Resonator Systems,” *IEEE Photonics Technology Letters,* vol. 14, no. 4, pp. 483-85, 2002.

[36] A. Yariv and Y. Pochi, Photonics: Optical Electronics in Modern Communications, Oxford , 2007.

[37] M. Yun, Y. Wan, J. Liang, F. Xia, M. Liu and L. Ren, “Multi-channel Biosensor Based on Photonic Crystal Waveguide and Microcavities,” *Optik - International Journal for Light and Electron Optics ,* vol. 123, no. 21, pp. 1920-1922, 2012.